

Magnetar counterparts, kinematics and birth sites with HST and JWST

A. A. Chrimes^{1,2*}, J. D. Lyman³, A. J. Levan^{2,3}, A. Borghese^{4*}, J. H. J. de Bruijne¹, A. S. Fruchter⁵, M. G. Guarcello⁶, C. Kouveliotou^{7,8}, N. R. Tanvir⁹ and K. Wiersema¹⁰

¹ European Space Agency (ESA), European Space Research and Technology Centre (ESTEC), Keplerlaan 1, 2201 AZ Noordwijk, the Netherlands

e-mail: ashley.chrimes@esa.int

² Department of Astrophysics/IMAPP, Radboud University, PO Box 9010, 6500 GL Nijmegen, The Netherlands

³ Department of Physics, University of Warwick, Gibbet Hill Road, CV4 7AL Coventry, United Kingdom

⁴ European Space Agency (ESA), European Space Astronomy Centre (ESAC), Camino Bajo del Castillo s/n, 28692 Villanueva de la Cañada, Madrid, Spain

⁵ Space Telescope Science Institute, 3700 San Martin Drive, Baltimore, MD 21218, USA

⁶ Istituto Nazionale di Astrofisica (INAF) – Osservatorio Astronomico di Palermo, Piazza del Parlamento 1, 90134 Palermo, Italy

⁷ Department of Physics, The George Washington University, Corcoran Hall, 725 21st St NW, Washington, DC 20052, USA

⁸ GWU/Astronomy, Physics and Statistics Institute of Sciences (APSIS)

⁹ School of Physics and Astronomy, University of Leicester, University Road, Leicester, LE1 7RH, United Kingdom

¹⁰ Centre for Astrophysics Research, University of Hertfordshire, College Lane, Hatfield, AL10 9AB, United Kingdom

Received 12 March, 2026; accepted XXXXX

ABSTRACT

Aims. Magnetars are highly magnetised, isolated neutron stars with uncertain formation channels. They comprise a potentially significant fraction of the young neutron star population in the Milky Way, and are implicated in the explosion mechanisms of some of the most powerful explosions in nature. We aim to identify magnetars in the near-infrared with *Hubble* Space Telescope (HST) and *James Webb* Space Telescope (JWST) imaging, in order to measure their proper motions and search for their birth sites.

Methods. Candidate infrared counterparts are selected based on variability, colours and proper motions which are outliers with respect to other sources in the field. Precise proper motions are obtained by tying HST/WCF3 and JWST/NIRcam images to the *Gaia* absolute astrometric reference frame.

Results. We newly identify infrared counterpart candidates for PSRJ1622–4950, 1RXSJ 170849.0-400910 and CXOUJ164710.2-455216, representing a substantial increase in the population. The past trajectory of the 1RXSJ 170849.0-400910-associated source coincides with the supernova remnant G346.6-0.2. The transverse velocity distribution of magnetars is found to be marginally inconsistent with that of young pulsars, due primarily to a dearth of high velocity magnetars. A candidate birth site is identified inside the cone of possible past trajectories in nearly every case. We show, based on the inferred kinematic ages, that magnetar characteristic ages may frequently be lower than the true age, but caution that this result depends on the reliability of the birth site associations.

Conclusions. We conclude that magnetars are broadly similar in terms of their kinematics and birth sites to the wider Galactic neutron star population, consistent with magnetar formation being a common outcome of massive star core-collapse. However, tentative evidence for a dearth of high-velocity magnetars is emerging. If real, this may arise from physical differences in the progenitor population giving rise to magnetars, or from differences in their post-formation velocity evolution.

Key words. Stars: magnetars – Stars: neutron – Proper motions – Stars: kinematics and dynamics – ISM: supernova remnants

1. Introduction

Magnetars are isolated neutron stars with very high magnetic fields, typically 10–100 times stronger than pulsars. Due to their strong fields they spin down rapidly, and the population within the Milky Way exhibits slow rotation periods $P > 1$ s. Their electromagnetic emission exceeds that expected solely from their spin-down via magnetic braking, given P and \dot{P} , and is thought to be additionally powered by the decay of their intense magnetic fields (see e.g. Mereghetti et al. 2015; Turolla et al. 2015; Kaspi & Beloborodov 2017; Esposito et al. 2021; Igoshev et al. 2021, for reviews). They have young characteristic ages of $< 10^5$ yr, as inferred from P and \dot{P} under the assumption of magnetic braking, a constant dipolar field and braking index $n = 3$ (e.g. Hamil

et al. 2015). Around ~ 30 have been directly observed, predominantly in the plane of the Milky Way, plus a few in the Magellanic Clouds (Olausen & Kaspi 2014).

Most known magnetars have thus far been discovered through high-energy outbursts (Coti Zelati et al. 2018) or flares (e.g. Mazets et al. 1979; Kouveliotou et al. 1999; Palmer et al. 2005; Negro et al. 2024), some of which can be luminous enough to be detected over extragalactic distances (Burns et al. 2021; Mereghetti et al. 2024). Historically, magnetars were labelled as anomalous X-ray pulsars (AXPs) or soft gamma repeaters (SGRs) based on their observational properties, but are now understood to be manifestations of the same physical objects (e.g. van Paradijs et al. 1995; Thompson & Duncan 1996; Kouveliotou et al. 1998).

* ESA Research Fellows

Follow-up of Galactic magnetars often reveals multi-wavelength counterparts, from ubiquitous quiescent X-ray emission to several optical-infrared counterparts (e.g. Tam et al. 2004; Morii et al. 2005; Testa et al. 2008; Dhillon et al. 2011; Levan et al. 2018) and a handful of radio detections (Camilo et al. 2006, 2008; Levin et al. 2010; Shannon & Johnston 2013; Esposito et al. 2020).

Magnetars are known to be variable at X-ray and optical/near-infrared (NIR) wavelengths. In some cases variations in the NIR flux appear to correlate with X-ray activity (e.g. Kern & Martin 2002; Tam et al. 2004; Israel et al. 2005; Dhillon et al. 2005; Chrimes et al. 2025), in others not (e.g. Durant & van Kerkwijk 2005, 2006b; Lyman et al. 2022). This variability is in any case a useful tool for identifying NIR counterparts: given crowded sight-lines in the Galactic plane and relatively large positional uncertainties from X-ray observations, identifying if one of a number of NIR candidates is variable is an effective way to unambiguously identify the counterpart (e.g. Israel et al. 2002, 2005).

Magnetars are also typically redder than field stars at NIR wavelengths (e.g. Chrimes et al. 2022b). The optical-IR flux is likely non-thermal and magnetospheric in origin, given the correlation with X-ray emission seen in some cases, and the power-law spectral energy distribution (SED) seen in 4U 0142+61 (Muñoz-Darias et al. 2016; Hare et al. 2024). However, this object appears spectrally variable on a timescale of years, and was previously observed to have a NIR bump in the SED consistent with blackbody emission from a debris disk (Wang et al. 2006; Ertan et al. 2007).

Magnetars are often kinematically distinct with respect to the objects in the surrounding field (e.g. Helfand et al. 2007; Tendulkar et al. 2012, 2013). As neutron stars, they have likely received large natal kicks imparting velocities which are much greater than the velocity dispersion and bulk motion of field stars (e.g. Hobbs et al. 2005; Verbunt et al. 2017; Igoshev 2020; Disberg et al. 2024; Disberg & Mandel 2025). Determining the proper motions of magnetars, and hence their transverse velocities if a distance can be measured or estimated, allows us to determine their natal kick distribution, and ultimately their birth sites by tracing back their motion. This is possible thanks to their young ages. There are several examples of magnetars associated with supernova remnants (SNRs) and stellar clusters (e.g. Muno et al. 2006; Gelfand & Gaensler 2007; Anderson et al. 2012; Lyman et al. 2022); the latter also enables progenitor mass estimates based on the age of the cluster (Davies et al. 2009; Ritchie et al. 2010).

There are two main ideas for how magnetars obtained their extreme magnetic fields: either through magnetic flux conservation during the core-collapse process (the ‘fossil field’ hypothesis, Woltjer 1964; Ferrario & Wickramasinghe 2006; Schneider et al. 2020), or through a dynamo upon neutron star formation (Thompson & Duncan 1993; Obergaulinger et al. 2014; Mösta et al. 2015; White et al. 2022; Reboul-Salze et al. 2022). The recent discovery of a Wolf-Rayet star with a magnetic field strong enough for magnetar formation suggests that the inherited fossil field scenario is plausible (Shenar et al. 2023), while the explanation of some high-energy extragalactic transients with (millisecond) magnetar central engines (e.g. gamma-ray bursts and superluminous supernovae, Gompertz et al. 2014; Metzger et al. 2015; Omand & Sarin 2024) is in favour of their rapid rotation at birth. However, there is no evidence of additional energy injection into the SNRs surrounding Galactic magnetars due to post-birth spin down of a rapidly rotating neutron star (Vink & Kuiper 2006). Indeed, population synthesis studies suggest that the population

of Galactic magnetars were likely not born with sufficient rotational energy to power such high energy transients (Rea et al. 2015). It is notable that not every Galactic magnetar has a clear SNR or cluster association (e.g. Tendulkar et al. 2013; Chrimes et al. 2025), despite their young characteristic (spin-down) ages.

Another class of transients linked with magnetars are fast radio burst (FRBs), particularly since the detection of FRBs from the Galactic magnetar SGR 1935+2154 (CHIME/FRB Collaboration et al. 2020; Bochenek et al. 2020). If the FRB-magnetar association is universal, the subsequent discovery of FRBs in a globular cluster (Kirsten et al. 2022) and ancient elliptical galaxies (Sharma et al. 2023) may point towards some fraction of magnetar formation through non-core-collapse channels with long delay times, such as the accretion or merger induced collapse of white dwarfs (Nomoto & Kondo 1991; Levan et al. 2006; Margalit et al. 2019).

Magnetar velocities and birth sites can be compared with the wider (young) neutron star population. In this way we can discern any differences in their progenitor systems, or otherwise (e.g. Hu & Zhang 2025). High resolution NIR imaging is ideally suited for this task. Measuring proper motions with even the highest resolution X-ray imaging is challenging (but possible for high proper motion objects or over long baselines, Kaplan et al. 2009; Rigoselli et al. 2024), and only a handful of Galactic magnetars are radio-bright (and hence amenable to radio interferometry, Helfand et al. 2007; Deller et al. 2012; Ding et al. 2020, 2024). Efforts have successfully been made with ground-based NIR observations assisted by adaptive optics (Tendulkar et al. 2012, 2013), but challenging absolute astrometry and the sensitivity of such observations is a limitation.

In this paper, we identify near-infrared (NIR) magnetar counterparts in repeat *Hubble* Space Telescope (HST) imaging by searching for red, variable and kinematically distinct sources consistent with magnetar X-ray localisations. In one case, these observations are supplemented by *James Webb* Space Telescope (JWST) imaging. By measuring the proper motions of magnetar NIR counterparts with respect to previous imaging, new constraints on the velocity distribution, birth sites and kinematic ages of several Galactic magnetars are obtained.

The paper is structured as follows. In Section 2 we describe the HST and JWST data used, the data reduction and the magnetars in our sample. Section 3 outlines the methodology including photometry, astrometry, proper motion measurement and counterpart identification. Section 4 presents the results including three new magnetar counterparts, transverse velocities and birth site identifications. A discussion and conclusions follow in sections 5 and 6. Magnitudes are reported throughout in the AB system (Oke & Gunn 1983), and uncertainties are stated at 1σ confidence unless otherwise stated.

2. Observations and data reduction

2.1. Hubble Space Telescope

The new HST observations used in this work (program GO 17927, PI: Chrimes) are summarised in Table 1. All observations were taken with the Wide Field Camera 3 (WFC3 Kimble et al. 2008) and each observation consists of either 3 or 4 dithered exposures. The sample comprises 15 magnetars for which at least one candidate counterpart was identified in previous HST observations (Chrimes et al. 2022b). Also listed are any previous epochs of HST observations, the filters used and the program IDs of those observations. We reduced the data following stan-

standard ASTRODRIZZLE procedures (Fruchter & Hook 2002)¹. The calibrated `_FLT` files for each image, which have undergone flat fielding and dark subtraction, were drizzled with a final orientation north up/east left, a `PIXFRAC` of 0.8 and a final pixel scale of $0.065 \text{ arcsec pixel}^{-1}$.

2.2. JWST

Two objects in our sample have been imaged with JWST: 4U0142, as part of a campaign specifically designed to study the magnetar, and CXOUJ1647, whose location was covered by JWST imaging of the Westerlund 1 stellar cluster (Guarcello et al. 2025). A detailed JWST study of 4U0142 has already been published by Hare et al. (2024). However, as the observations were taken with the SUB400P sub-array, the field of view is small and there are no reference sources we can use for astrometry (and hence a proper motion measurement) in the images.

CXOUJ1647 on the other hand was imaged as part of a large mosaic covering the Westerlund 1 cluster (program GO 1905, PI: Guarcello). For this magnetar we have 2 previous epochs of F140W HST imaging, a 2026 epoch of F125W and F160W, plus imaging in 8 JWST wide filters (5 NIRcam and 3 MIRI, all obtained in 2023). We use the NIRcam/F150W image for the proper motion measurements, and make use of the DOLPHOT catalogue produced by Guarcello et al. (2025, see next section).

2.3. Sample summary

Our final sample consists of 14 objects with at least two epochs of space-based imaging. These are the 15 objects listed in Table 1, minus SGR 1806 whose 2025 epoch is the first set of HST images for this object. All remaining objects have two HST epochs (taken in 2018/2020 and 2025) with the exceptions of SGR 0501 (three epochs of HST between 2010 and 2025), SGR 1935 (five epochs of HST between 2015 and 2025) and CXOUJ1647 (four epochs, $3 \times \text{HST}$ and $1 \times \text{JWST}$ spanning 2017–2026).

In Figure 1 we show image cutouts (‘stamps’) around the position of each magnetar. The approximate 3σ X-ray error circle is plotted in each case (assuming Gaussian uncertainties and based on positions reported in the McGill magnetar catalogue, Olausen & Kaspi 2014, we note that none of the 14 objects in our sample have a position measured with radio interferometry)². Sources which we identify as NIR counterparts to magnetars, based on the criteria outlined in the next section, are circled in red.

3. Methodology

3.1. Photometry

We carry out source detection and photometry for all HST images using DOLPHOT (Dolphin 2000, 2016; Weisz et al. 2024)³ with the point spread functions of Anderson (2016). The detection thresholds for point sources were set at 3σ . Source detection was performed using only the individual `_FLT` frames, with photometry of detected sources performed on both these and the drizzled `_DRZ` images. Magnitudes are converted to the AB system using conversions calculated with STSYNPHOT⁴.

¹ Available with DRIZZLEPAC, <https://www.stsci.edu/scientific-community/software/drizzlepac>

² <https://www.physics.mcgill.ca/~pulsar/magnetar/main.html>

³ <http://americano.dolphinim.com/dolphot/>

⁴ https://github.com/spacetelescope/stsynphot_refactor

These conversions (added to Vega magnitudes to obtain AB) are 0.9204 (F125W), 1.0973 (F140W), 1.2277 (F150W) and 1.2741 (F160W). For the JWST observations of CXOUJ1647 we use the existing DOLPHOT output catalogue of sources in and around Westerlund 1 produced by Guarcello et al. (2025), as described in that paper. Additions to the JWST/NIRcam Vega magnitudes are 0.7949 (F115W), 1.2277(F150W), 1.7014 (F200W), 2.3160 (F277W) and 4.3664 (F444W) (Rodrigo & Solano 2020)⁵.

3.2. Astrometry and proper motions

By measuring the relative offset of a source in images taken some time apart, with respect to the surrounding objects in the field, we can measure its proper motion. We adopt a method described in detail by Bedin & Fontanive (2018) and Lyman et al. (2022), but briefly summarise it here. Starting from the DOLPHOT source catalogues, we first perform quality cuts (removing objects which are not point sources or are overly crowded, as outlined by Lyman et al. 2022). *Gaia* sources within the HST/WFC3 field of view are then selected (using *Gaia* data release 3, Gaia Collaboration et al. 2023), and sources with a poor astrometric solution (a renormalised unit weight error, or RUWE > 1.2 , Penoyre et al. 2022) are removed. The *Gaia* positions were then offset, using their proper motions where available, to obtain their expected positions at the time of each HST observation. These shifted positions (in equatorial coordinates) are then transformed first into a tangent plane, and then to HST pixel (x,y) coordinates using the existing world coordinate system of the images (which itself has been determined through an astrometric tie with *Gaia*). The x,y coordinates of the shifted *Gaia* sources are then matched with the HST source catalogues by identifying the closest match to each *Gaia* source. Outliers in the resulting offset distribution for the matching pairs (above the 95th percentile) are rejected. A new (x,y) to (α, δ) transformation is then fit following Bedin & Fontanive (2018), where the uncertainty in this transformation represents the absolute astrometric uncertainty.

This method yields absolute astrometry at a comparable level to HST-only relative astrometry (Lyman et al. 2022, typically several tens of milliarcseconds). The uncertainty on the resulting proper motion of a given source has contributions from both the absolute astrometric uncertainty and the positional uncertainty of the source (i.e. how well its centroid can be measured, which is proportional to the signal-to-noise). Because we have DOLPHOT catalogues containing positions for all sources in the images above a detection threshold, we can plot, for any pair of images, the difference in α, δ between sources which are detected in both images. This is shown in Figures 2, 3, 4, 5. Sometimes we are comparing the positions of objects in images taken just minutes apart (e.g. two images with different filters in the same HST orbit). In this case, the scatter is centred on 0,0 and simply reflects the astrometric uncertainties. When the images are taken several years apart, the bulk motion of stars in the field is evident as a shift in the clouds of points. This apparent bulk motion can arise from both the differential rotation between our position in the Galaxy and along the sight-line in question; and the ‘real’ motion of stars in their local standard of rest (e.g. moving groups). When reporting proper motions in Section 4, we first account for the differential rotation (and Solar velocity with respect to the local standard of rest, LSR, Ding et al. 2019) following Verbunt et al. (2017); Lyman et al. (2022). The reported proper motions are therefore proper motions with respect to the LSR at the assumed distance of the magnetar (see Table 3), i.e.,

⁵ The SVO filter profile service

Table 1. Details of the *Hubble* Space Telescope observations taken under program 17927. Previous epochs of HST observations are listed in the final two columns. All observations use HST WFC3/IR and the F125W, F140W or F160W NIR filters, with the exception of the JWST/NIRcam observations of CXOUJ1647. For each magnetar there is one row per filter (with observations in GO 17927 and previous programs given where available), unless there are multiple epochs of imaging in that filter. Dashes indicate a lack of observations in that filter (either in GO 17927 or previous programs). Shortened magnetar names are indicated in the first column, which are subsequently used throughout for brevity.

Magnetar	Epoch	Start date/time [UT]	Exptime [s]	Filter	Prev. epoch(s)	Program ID of prev. epoch(s)
PSRJ1622(-4950)	2025.2	2025-02-28 06:26:40	1058.819	F125W	2020.7	16019
	2025.2	2025-02-28 06:47:25	1058.819	F160W	2020.7	16019
SWIFT J1822(.3-1606)	2025.2	2025-03-30 19:53:25	1058.819	F125W	2018.5	15348
	2025.2	2025-03-30 20:14:10	1058.819	F160W	2018.5	15348
SWIFT J1834(.9-0846)	2025.2	2025-03-30 21:27:23	1058.819	F125W	2020.2	16019
	2025.2	2025-03-30 21:48:08	1058.819	F160W	2020.2	16019
SGR1627(-41)	2025.3	2025-04-24 14:32:17	1058.819	F125W	2020.7	16019
	2025.3	2025-04-24 14:53:02	1058.819	F160W	2020.7	16019
1RXS J1708(49.0-400910)	2025.3	2025-05-06 14:17:49	1058.819	F125W	2018.8	15348
	2025.3	2025-05-06 16:13:18	1058.819	F160W	2018.8	15348
CXOUJ1714(05.7-381031)	2025.3	2025-05-06 15:52:33	1058.819	F125W	2018.3	15348
	2025.3	2025-05-06 16:13:18	1058.819	F160W	2018.3	15348
SGR1900(+14)	2025.4	2025-05-26 15:38:49	1058.819	F125W	2020.7	16019
	2025.4	2025-05-26 15:59:34	1058.819	F160W	2020.7	16019
SGR1806(-20)†	2025.4	2025-06-03 18:37:11	1058.819	F125W	-	-
	2025.4	2025-06-03 18:57:56	1058.819	F160W	-	-
AX J1818(.8-1559)	2025.4	2025-06-04 11:59:48	1058.819	F125W	2018.6	15348
	2025.4	2025-06-04 12:20:33	1058.819	F160W	2018.6	15348
1E2259(+586)	2025.4	2025-06-15 01:29:31	1058.819	F125W	2018.6	15348
	2025.4	2025-06-15 01:50:16	1058.819	F160W	2018.6	15348
SGR 1833(-0832)	2025.5	2025-06-16 06:56:38	1058.819	F125W	2018.5	15348
	2025.5	2025-06-16 08:30:27	1058.819	F160W	2018.5	15348
SGR1935(+2154)	2025.5	2025-06-30 16:54:07	1058.819	F125W	-	-
	2025.5	2025-06-30 17:14:52	1058.819	F160W	-	-
SGR0501(+4516)	-	-	-	F140W	2021.4	16505
	-	-	-	F140W	2016.4	14502
	-	-	-	F140W	2015.6	14055
	-	-	-	F140W	2015.2	14055
	2025.6	2025-08-14 01:39:26	1058.819	F125W	2020.6	16019
4U0142(+61)	2025.6	2025-08-14 02:00:11	1058.819	F160W	2020.6	16019
	-	-	-	F160W	2012.8	12672
	-	-	-	F160W	2010.8	12306
	2025.5	2025-06-29 01:59:10	1058.819	F125W	2018.0	15348
CXOUJ1647(10.2-455216)	2025.5	2025-06-29 02:19:55	1058.819	F160W	2018.0	15348
	-	-	-	F140W	2017.4	14805
	-	-	-	F140W	2018.4	14805
	-	-	-	F115W (JWST)	2023.2	1905
	-	-	-	F150W (JWST)	2023.2	1905
	-	-	-	F200W (JWST)	2023.2	1905
	-	-	-	F277W (JWST)	2023.2	1905
	-	-	-	F444W (JWST)	2023.2	1905
2026.1	2026-02-04 23:15:52	1058.819	F125W	-	-	
2026.1	2026-02-04 23:29:42	1058.819	F160W	-	-	

† - Previous epochs for SGR1806 suffered from guide star acquisition failure, resulting in unusable data.

they are peculiar proper motions. The impact of the large distance and hence velocity uncertainties are explored in Section 5).

3.3. Counterpart identification

To identify NIR counterparts, we follow an established methodology of searching for objects in the magnetar X-ray error circles which are discrepant from objects in the field in terms of proper motion, colour and variability. This is particularly useful

in crowded fields with multiple candidates, and because magnetars are faint (and potentially undetected) at these wavelengths. In most cases we have 2 HST epochs, with F125W and F160W imaging in each. In Figures 2, 3, 4 and 5 we plot the difference in the $\alpha\cos(\delta), \delta$ position of objects which are matched between the images. In the standard case this gives us one panel where the two images are taken minutes apart (same epoch, different filters). In these panels, the colourmap represents the F125W-F160W colour, and the $\Delta\alpha, \Delta\delta$ scatter solely reflects astrometric noise. We also have panels showing $\Delta\alpha, \Delta\delta$ for pairs of F125W

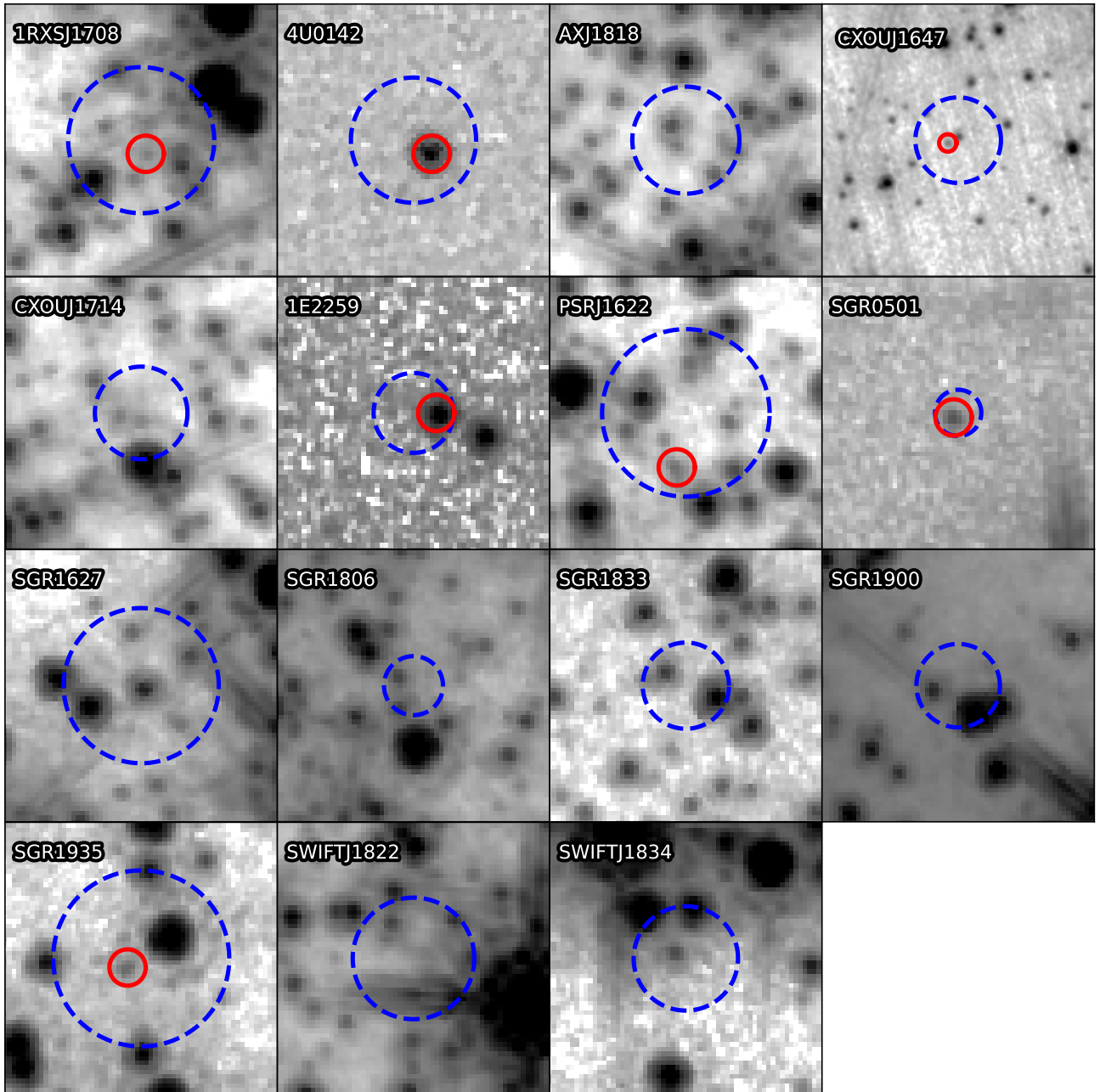


Fig. 1. HST cutouts with magnetar 3σ X-ray localisations indicated by blue dashed circles (from Olausen & Kaspi 2014, and references therein). If a counterpart candidate is identified, its position is indicated by a red circle. Only the latest (2025 epoch) F160W images are shown, with the exception of CXOUJ1647 (which is a 2023 JWST/NIRcam F150W image). Each cutout measures 4×4 arcsec, and they are oriented North up, East left.

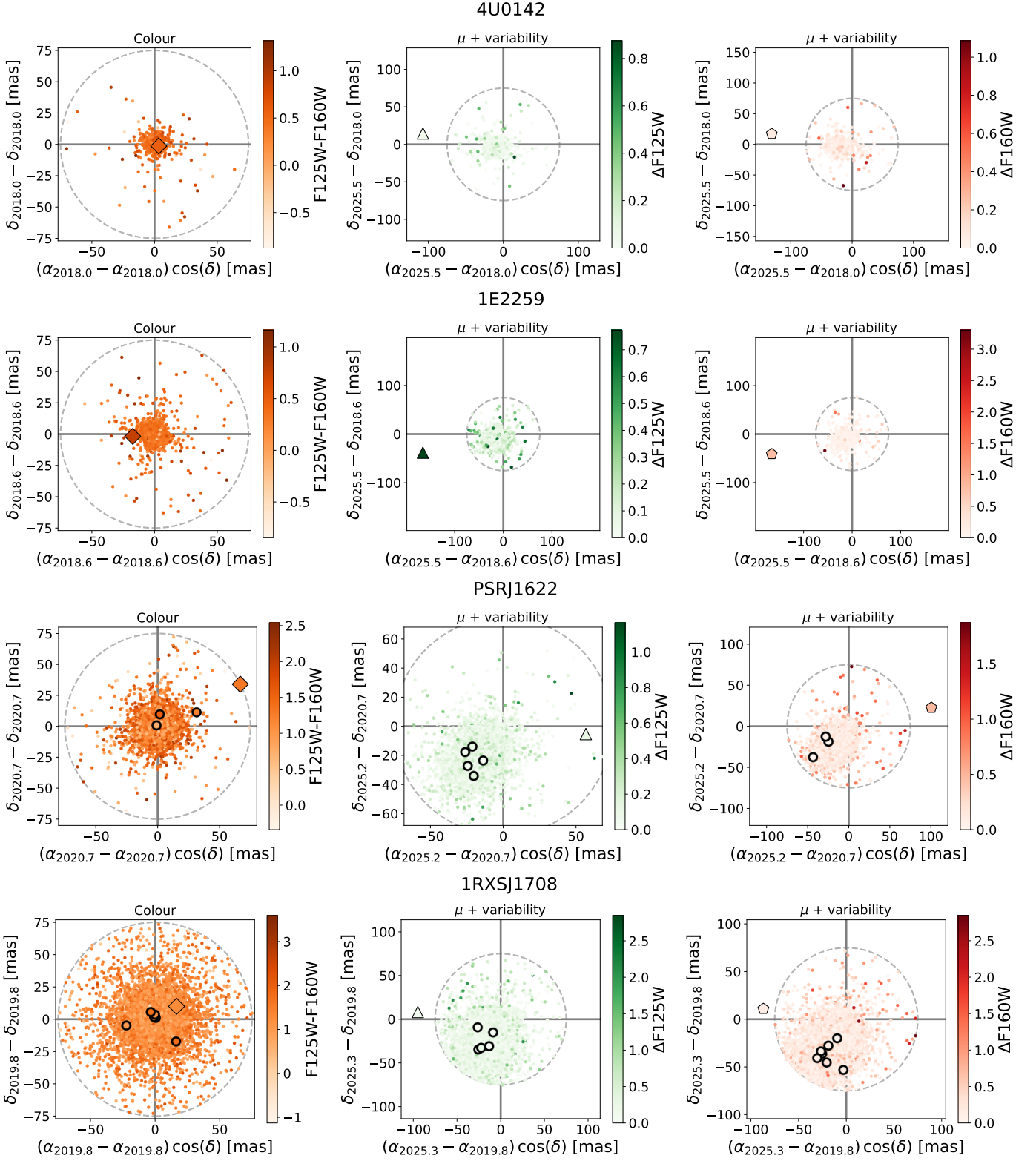


Fig. 2. For the cases where a good candidate was identified in the 3σ error circle based on distinct kinematics, colour and/or variability, and four epochs were available. Counterparts are labelled with diamonds/triangles/pentagons, other objects in the X-ray localisation regions are labelled as circles with bold outlines. Left panel: comparing images taken minutes apart, here we are seeing the astrometric noise. The points correspond to objects detected in both images and are coloured according to their F125W-F160W colour. Middle: the movement of sources between the first and second epochs of F125W imaging. The bulk motion of sources in the field is clear, while the magnetar counterparts tend to stand apart from this systemic drift due to their large natal kicks. The points are coloured by the difference in F125W between the epochs. Right: as for the middle panel, but the difference between the two epochs in F160W. The derived proper motions and their uncertainties are provided in Table 3.

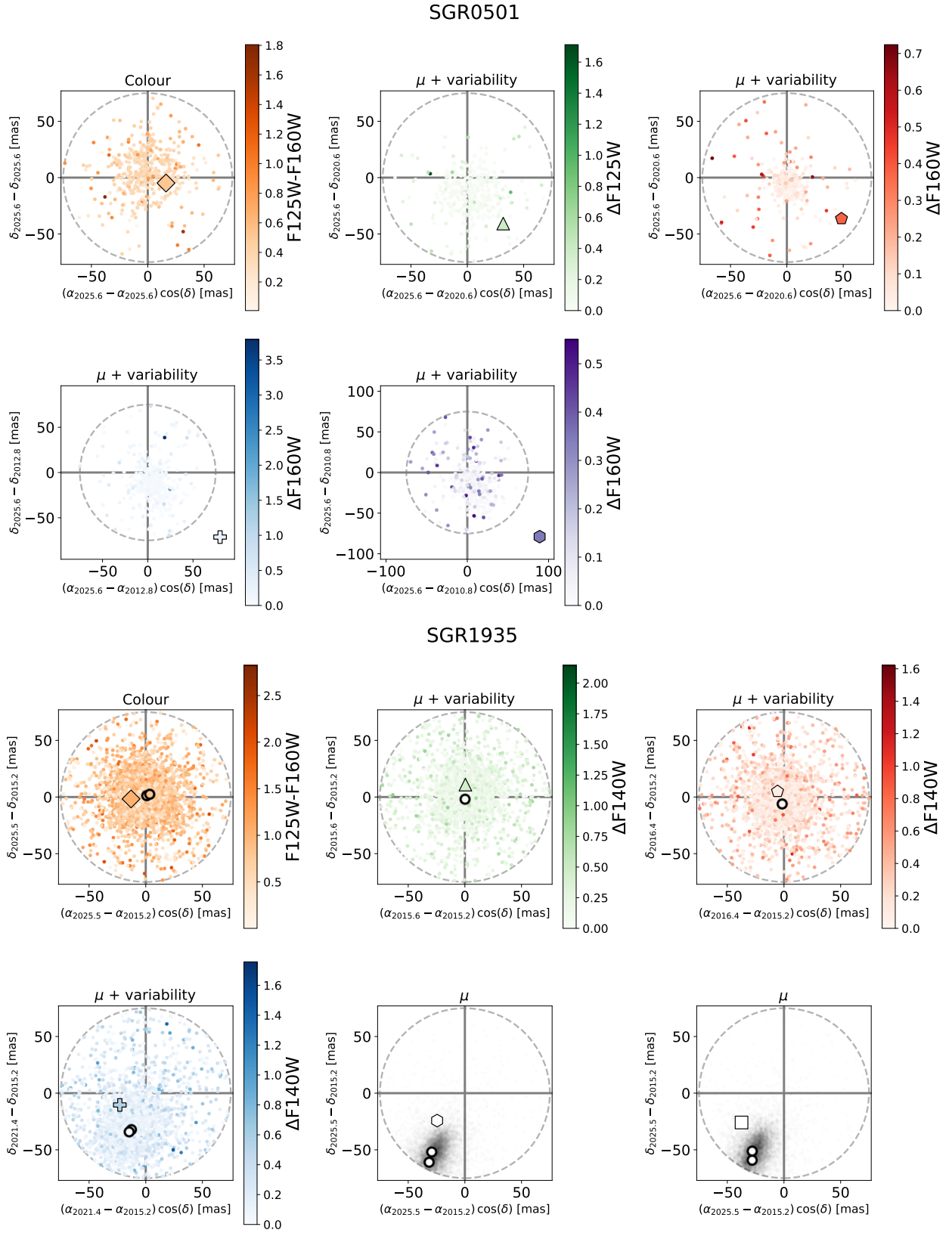


Fig. 3. As in Figure 2, but for the cases where six images were available. The μ -only panels for SGR 1935 compare different filters, F140W versus F125W (the panel with SGR 1935 marked with a hexagon) and F160W (SGR 1935 marked with a square).

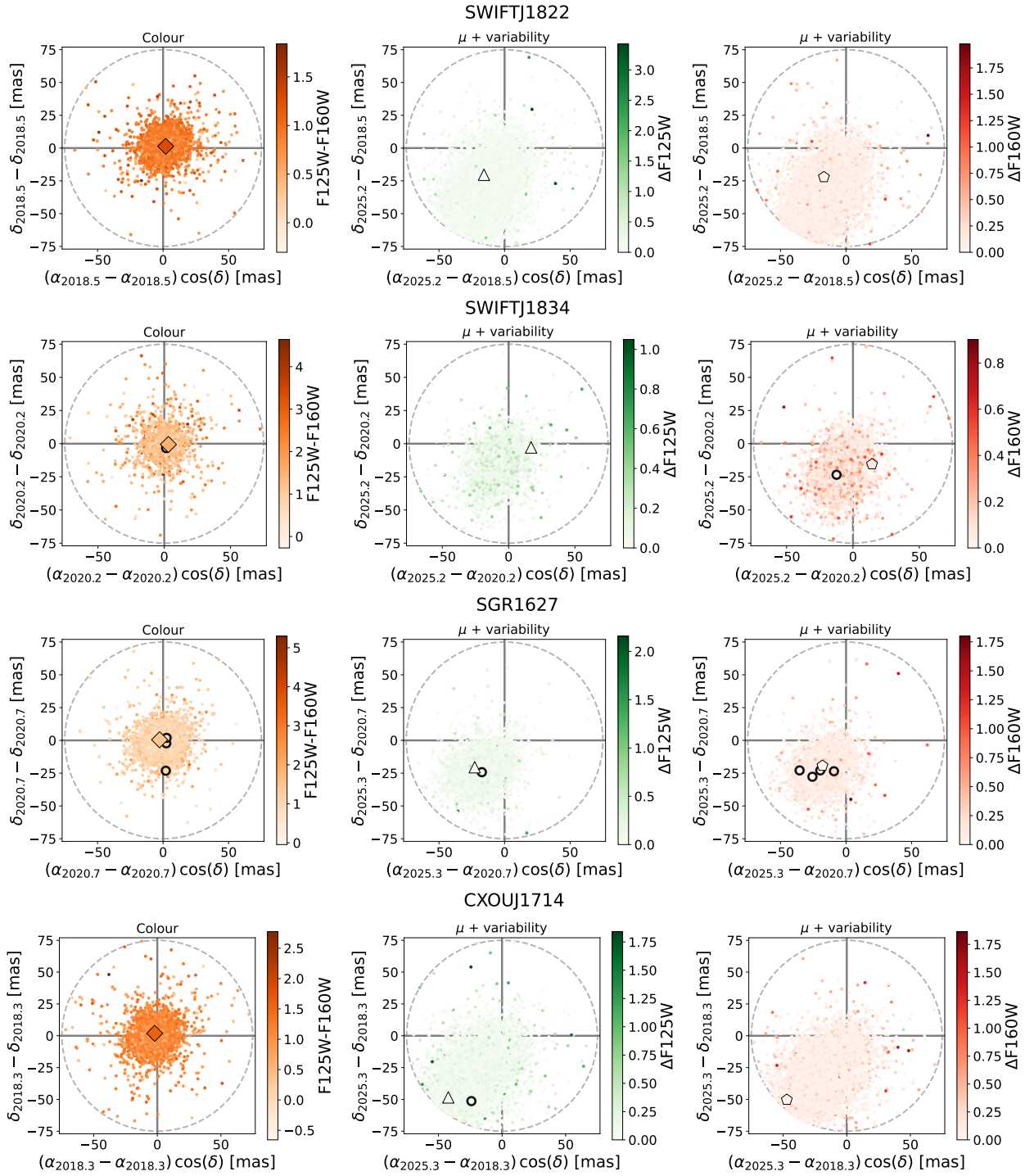


Fig. 4. As in Figures 2 and 3, but for the cases where no good candidate was identified in the 3σ error circle based on distinct kinematics, colour and/or variability. The sources marked with diamonds/triangles/pentagons are the candidates selected solely on P_{chance} grounds by Chimes et al. (2022b), the P_{chance} values are (top to bottom) 0.15, 0.05, 0.03 and 0.005.

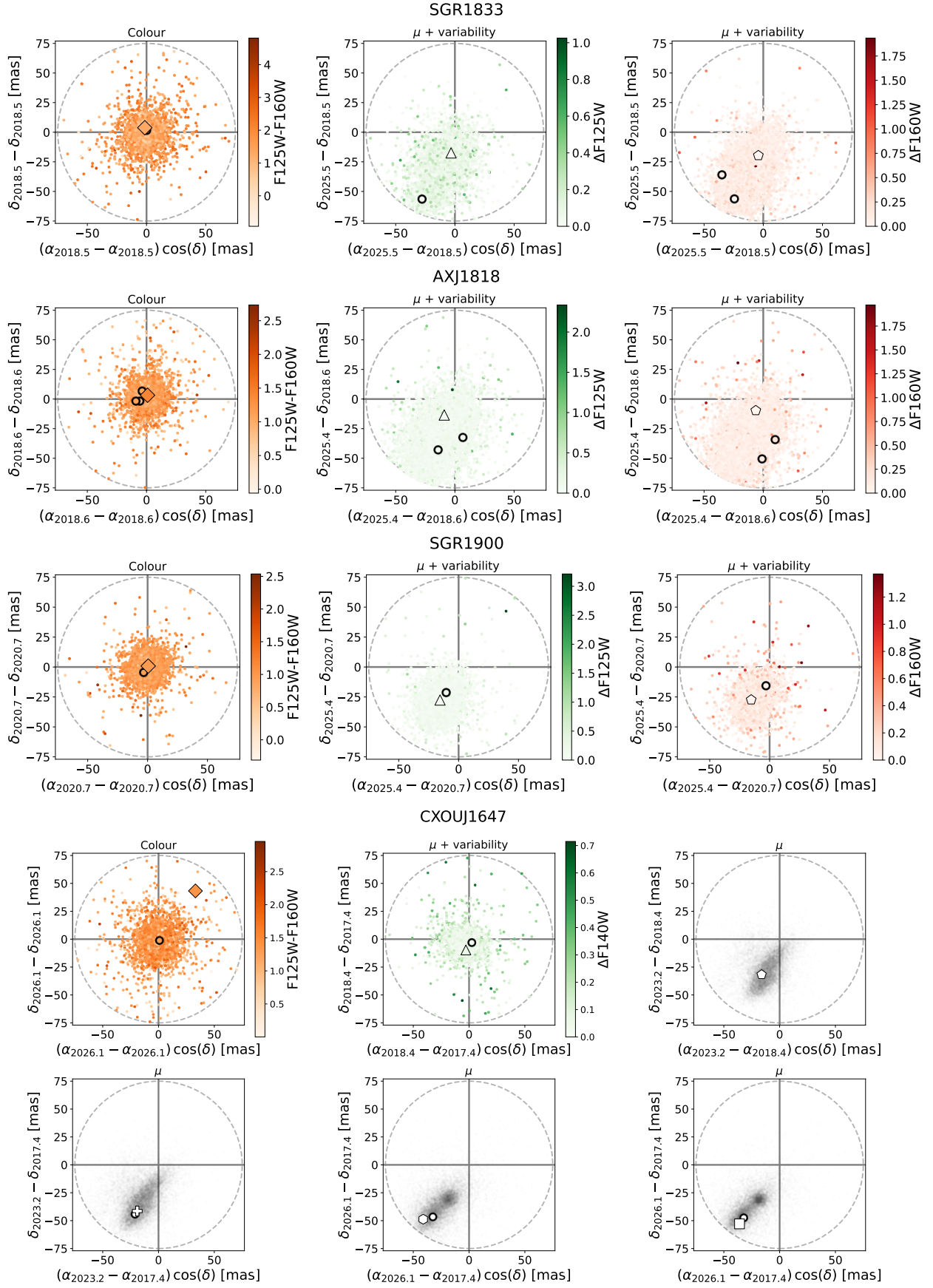


Fig. 5. Figure 4 continued. More cases where no good candidate was identified in the 3σ error circle based on distinct kinematics, colour and/or variability. The sources marked with diamonds/triangles etc. are simply the candidates identified on P_{chance} grounds by Chrimes et al. (2022b), the P_{chance} values are (top to bottom) 0.03, 0.18, 0.03 and 0.45. The last two panels for CXOUJ 1647 compare the first epoch in 2017 (F140W) with the F125W and F160W images taken in 2026. We use the F150W JWST/NIRcam image for the 2023 epoch.

and F160W images, obtained years apart. Here the colour scale represents variability instead (i.e. $\Delta F125W$, $\Delta F160W$), and the distribution in $\Delta\alpha$, $\Delta\delta$ parameter space has contributions from both noise and proper motion as described in the previous section. In every panel of these figures, objects inside the 3σ X-ray error circles are indicated by circles with bold outlines, and the best counterpart candidate in each case is denoted by other shapes (diamonds, triangles, pentagons, crosses, hexagons and squares).

To classify an object as a counterpart candidate, we require either (i) at least one of the proper motion, colour or variability to be $>3\sigma$ outside the scatter in the field objects, in at least one epoch or (ii) two or more of proper motion, colour or variability to be $>2\sigma$ outliers. Figures 2 and 3 show the magnetars where a kinematically distinct, red and/or variable object was found in the X-ray error circle. Six objects in our sample meet these criteria 4U 0142 and 1RXSJ 1708 pass purely on their discrepant proper motion, SGR 1935 passes on variability alone, SGR 0501 and PSR J1622 passes on both proper motion and variability, and 1E 2259 passes on all three criteria. In every case the parameter on which the selection is made exceeds 3σ . Of these, the counterparts of 4U 0142, 1E 2259, SGR 0501, SGR 1935 were already known, further supporting the validity of the method. We additionally report new NIR counterparts for PSR J1622 and 1RXSJ 1708.

4U 0142, 1E 2259, PSR J1622 and 1RXSJ 1708 have just two epochs of two-filter HST imaging. SGR 0501 has four epochs of observation, the first two solely in F160W and last two in both F125W and F160W. Using the 2025 epoch as the reference we therefore have three $\Delta F160W$, one $\Delta F125W$ and one F125W-F160W panel. The known counterpart of SGR 0501 clearly stands out in terms of kinematics and variability. SGR 1935 has five epochs: four in which the sole filter was F140W, and 2025 with F125W and F160W. Here we take the first epoch (2015) as the reference, showing in Figure 3 $\Delta F140W$ for three panels, ($\Delta\alpha$, $\Delta\delta$) only for the fourth (we cannot disentangle colour/variability when comparing F125W/F160W with F140W images taken years before), and finally the 2025 F125W-F160W colour. The motion of SGR 1935 is clearly visible in the final two panels of Figure 3.

The rest of the sample is shown in Figures 4 and 5. In these cases, none of the sources in the X-ray localisation meet the selection criteria, so we cannot confidently claim to have identified the counterpart. The ‘best candidate’ in Figures 4 and 5 is labelled as such purely on the chance alignment probability (i.e. they are the brightest sources in the error circle).

4. Results

We present apparent magnitudes and LSR-corrected proper motions for the six identified counterparts in Tables 2 and 3. The latter also includes a distance estimate for the magnetar, and the resulting peculiar transverse velocity v_t at that distance. Near-IR HST light-curves for the six objects are provided in Figure A.1 of the Appendix, including photometry on the individual $_{FLT}$ level images, which have undergone calibrations including flat fielding and dark subtraction, but have not yet been combined with the drizzling process. Some level of variability is apparent in most of these sources, even those which were not selected on this criteria (e.g. SGR 0501). Notes on individual objects for which we report a new counterpart candidate, fail to recover a previously known counterpart, or successfully ‘re-discover’ a known source, are provided in the following subsections.

4.1. Recovered known counterparts

We successfully recover the known NIR counterparts of 1E 2259 (Hulleman et al. 2001; Tam et al. 2004; Tendulkar et al. 2013), 4U 0142 (Hulleman et al. 2004; Wang et al. 2006; Hare et al. 2024), SGR 1935 (Levan et al. 2018; Lyman et al. 2022) and SGR 0501 (Dhillon et al. 2011; Chrimes et al. 2025). These objects all have a previously measured proper motion, which are provided for reference in Table A.1 of the Appendix, and we reduce the uncertainties further by moving to space-based observations and/or extending the temporal baseline.

4.2. Unrecovered known counterparts

4.2.1. SGR1806-20

The 2025 epoch imaging presented in this paper is the first space-based imaging of SGR 1806, although a magnitude 23–34, variable K_s -band counterpart was identified by Israel et al. (2005); Kosugi et al. (2005) and subsequently in ground-based Very Large Telescope (VLT) and Keck imaging Tendulkar et al. (2012). There is no detected source at the position of the source labelled A by Israel et al. (2005); Tendulkar et al. (2012) in the 2025 F125W and F160W images. There is however a slightly offset source present in the F160W images (the closest in terms of wavelength) which lies between the position of SGR 1806 in 2004 and the star to the south-west which Israel et al. (2005); Tendulkar et al. (2012) labelled C. Assuming this is SGR 1806 and comparing its position with the reported 2004 coordinates, it would have a proper motion of $\sim 10 \text{ mas yr}^{-1}$, higher than the value of $\sim 5 \text{ mas yr}^{-1}$ reported by Tendulkar et al. (2012) and in an approximately perpendicular direction. We therefore assume that the F160W source is not related, and that SGR 1806 is not detected in our F125W and F160W imaging. The high extinction along the sight-line means that our imaging, even in the longer F160W filter, could reduce the counterpart flux as much as 6 magnitudes (for a flat spectrum and $A_V \sim 30$ Eikenberry et al. 2004) versus the 23–34 K_s -band magnitude, plausibly explaining our non-detection.

4.2.2. SGR1900+14

The infrared counterpart of SGR 1900 was previously identified in VLT/NACO (Testa et al. 2008) and Keck/NIRC2 (Tendulkar et al. 2012) K_s -band imaging, using adaptive optics for enhanced spatial resolution which reached the \sim milli-arcsecond level. Comparing the images in those papers with Figure 1, we can see that the source is not detected in our imaging. This is likely due to the factor of ~ 10 lower spatial resolution and subsequent blending with the adjacent star, rather than variability, since our HST imaging has a limiting magnitude which is 5-6 magnitudes deeper. Higher resolution observations with current adaptive optics-assisted ground-based facilities, JWST, or future observatories such as the the European Extremely Large Telescope (Gilmozzi & Spyromilio 2007) would likely be required to re-detect the counterpart. In any case, this magnetar already has a proper motion measurement (Tendulkar et al. 2012, ,see Table A.1 in the appendix).

4.3. New counterpart candidates

4.3.1. PSRJ1622–4950

We report the discovery of a candidate infrared counterpart to PSRJ1622–4950. The object is one of four detected in the 3σ

X-ray error circle. It is kinematically distinct with a high proper motion, and shows variability (most notably in F160W). This is not the candidate identified by Chrimes et al. (2022b), which was simply selected based on P_{chance} arguments.

Levin et al. (2010) report a distance for PSRJ1622–4950 (and the associated SNR G333.9+0.0) of ~ 9 kpc (with an uncertainty of a factor of ~ 2), based solely on the radio dispersion measure using the NE2001 electron density model (Cordes & Lazio 2002). Placing the IR counterpart of PSRJ1622–4950 at 9 kpc, and correcting for the extinction at $1.6\mu\text{m}$ of 5.2 magnitudes (adopting a Fitzpatrick extinction law, Fitzpatrick 1999, and $R_V = 3.1$), we find the source is extremely blue, with an intrinsic absolute magnitude of $M_{\text{F160W}} \sim 3.5$. This is ~ 5 – 8 magnitudes brighter than other confirmed IR counterparts (e.g. Chrimes et al. 2022a). Placing it instead at 5.5 kpc, the distance implied by the YMW16 electron density model (Yao et al. 2017), and adopting approximately half the extinction as implied from the A_V - N_H relation (Predehl & Schmitt 1995), we find $M_{\text{F160W}} \sim 8$ which is more comparable with other counterparts. Overall, a distance of ~ 5 kpc brings PSR J1622–4950 into line with the rest of the population, and given the large uncertainty on the previous distance estimate, such a revision is plausible. We therefore suggest that this object (and its associated SNR) lie at ~ 5 kpc, adopting this revised distance throughout.

The position of PSR 1622 shows a systematic offset between the F125W and F160W filters (see Figure A.1 of the Appendix). This may be due to a faint, adjacent source which has affected the centroiding (and possibly also the flux measurement). However, the proper motion appears to be consistent between the two filters despite this offset, and is small nevertheless, so this does not affect our conclusion regarding the origin of PSR 1622 in SNR G333.9+0.0.

4.3.2. 1RXSJ170849-400910

We identify a new candidate counterpart to 1RXSJ1708 based on its unusual kinematics. This is not the first counterpart candidate for 1RXSJ1708, and it is neither of the brighter sources near the south-eastern edge of the X-ray error circle identified by Israel et al. (2003); Durant & van Kerkwijk (2006c). Although the counterpart claimed by Durant & van Kerkwijk (2006c) showed signs of variability (at 3σ significance), Chrimes et al. (2022a) showed that this source would have an intrinsic H -band absolute magnitude of ~ 5 , far brighter than that of securely identified counterparts (e.g. 4U 1042, SGR 0501). The 3.8 kpc distance to this magnetar is based on the optical extinction, which was first estimated from absorption edges in the magnetar X-ray spectra (and is consistent with the A_V - N_H relation Chrimes et al. 2022a), and the distance through the Galactic plane that this extinction implies (Durant & van Kerkwijk 2006c,a). At this distance, and with extinction $A_V = 7.6$, the new counterpart identified in this work would have absolute magnitude of ~ 8 . This is closer to the known population, and coupled with its discrepant kinematics with respect to field, we deem the faint source labelled in Figure 1 to be the likely counterpart.

4.3.3. CXOUJ164710.2-455216

Finally, we report the likely identification of the infrared counterpart of magnetar CXOUJ 1647, which lies outside the Westlund 1 massive star cluster (Muno et al. 2006). None of the HST sources in the X-ray error circle pass our counterpart selection by the stated criteria. This includes the object identified as a

Table 2. Photometry of the NIR counterparts reported in this work. For details of the observations, and previous HST epochs in these filters (or similar), see Table 1. CXOUJ1647 is not detected in the HST imaging, we list here the JWST/NIRcam photometry of Guarcello et al. (2025).

Magnetar	Epoch	Filter	m(AB)
4U0142	2025.5	F125W	22.71 \pm 0.01
	2025.5	F160W	22.17 \pm 0.01
SGR0501	2025.6	F125W	24.64 \pm 0.04
	2025.6	F160W	24.12 \pm 0.04
PSRJ1622	2025.2	F125W	24.47 \pm 0.05
	2025.2	F160W	23.52 \pm 0.03
SGR1935	2025.5	F125W	25.37 \pm 0.08
	2025.5	F160W	24.33 \pm 0.04
1E2259	2025.4	F125W	23.60 \pm 0.02
	2025.4	F160W	23.12 \pm 0.02
1RXSJ 1708	2025.3	F125W	24.71 \pm 0.05
	2025.3	F160W	23.77 \pm 0.03
CXOUJ1647	2023.2	F115W	25.57 \pm 0.20
	2023.2	F200W	23.45 \pm 0.04
	2023.2	F277W	22.77 \pm 0.02
	2023.2	F444W	22.14 \pm 0.01

candidate counterpart by Testa et al. (2018), which we will refer to as source A. However, in the deeper JWST imaging available for the field, a second source (B) detected close to the centre of the error circle. We find that the extinction-corrected ($A_V = 10$) SED of source B is well described by a power-law of the form $f_\nu \propto \nu^{-\alpha}$, with $\alpha = -0.5854 \pm 0.0003$. This compares with $\alpha = 2$ for the Rayleigh-Jeans tail of a black body, as expected for stellar SEDs. Given that power-law SEDs appear to be typical for magnetars at these wavelengths (Muñoz-Darias et al. 2016; Hare et al. 2024), the otherwise typically stellar SED of source A, and the unremarkable colours of the other candidates in the X-ray error circle, we deem source B the likely counterpart and label it as such in Figure 1. The SEDs of sources A and B are shown in Figure 6, but we leave a full multi-wavelength study of this magnetar to future work (Borghese et al., in prep). For the purposes of this paper, as source B is only detected in the JWST imaging, no proper motion measurement is possible without a second JWST epoch. This is one of only a few of magnetars thus far with a candidate former binary companion (Clark et al. 2014; Sherman et al. 2024), and the proper motion of this candidate former companion is well constrained by *Gaia*, so determining the past trajectory of CXOUJ 1647 is an important and viable test of their association.

4.4. Transverse velocities

For the six NIR counterpart identifications with proper motion measurements, figures visualising the fits are given in Figures A.2 and A.3 of the Appendix. We convert the peculiar proper motion into a transverse velocity by adopting the distances listed in Table 3. These six velocities are supplemented by XTE J1810 (Ding et al. 2020), 1E 1547 (Deller et al. 2012), SGR 1806 and SGR 1900 (Tendulkar et al. 2012) and Swift J1818 (Ding et al. 2024), for a total of 11 magnetars with transverse velocity measurements. The proper motions, distances and velocities of these additional six magnetars are provided in Table A.1 of the Appendix. The transverse velocity of SGR J1745 has also been measured (Bower et al. 2015), but it is likely bound to Sgr A*, so we do not consider it further.

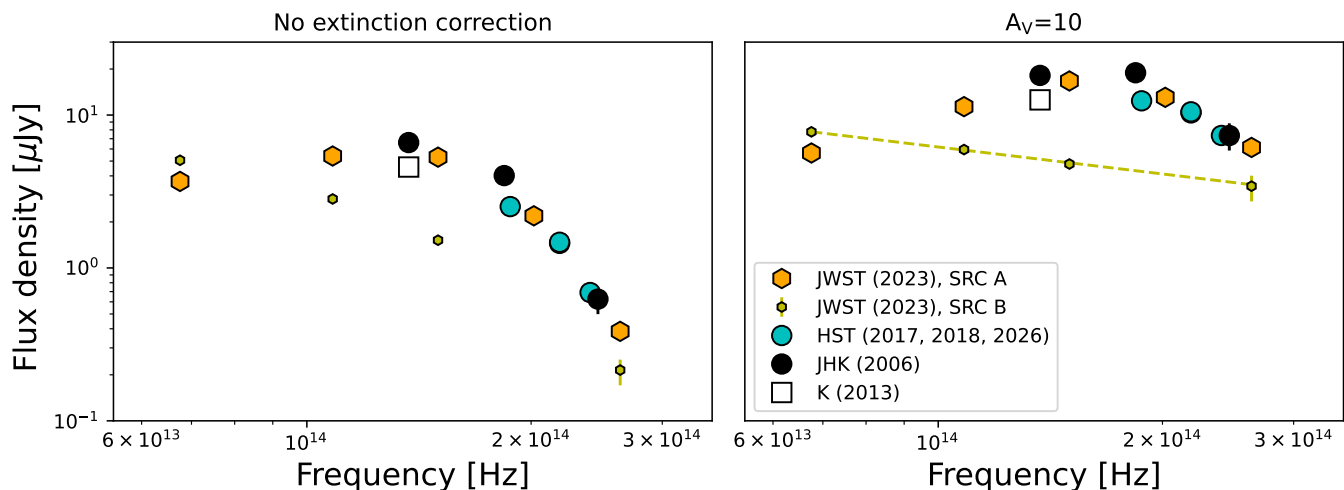


Fig. 6. The NIR spectral energy distribution (SED) of the two objects close to the centre of the X-ray localisation of CXOUJ1647. One is a source previously identified as a candidate counterpart (Testa et al. 2008), however the other has a power-law SED after extinction correction, similar to other known magnetar counterparts, so we deem this the likely counterpart. Measurements of the brighter, previously identified source are from Testa et al. (2018, for the 2006 JHK_s and 2013 K_s points), this work and Chrimes et al. (2022b, HST) and Guarcello et al. (2025, for the JWST/NIRcam data). Note that in Figure 5, neither of the objects in the X-ray error circle with a proper motion measurement are the power-law source, since it is not detected in the HST images.

The cumulative distribution of the 11 magnetar velocities is shown in Figure 7. We generate 1000 realisations of the distribution by sampling the proper motion uncertainties, assuming they are Gaussian. We note that distance uncertainties are not accounted for, and although these can be considerable (only two magnetars have a parallax measurement, Ding et al. 2020, 2024), they are hard to formally quantify. Each step in the distribution is labelled by the method through which the best available proper motion was measured. We note that parallaxes are unlikely to strongly influence our proper motion measurements: for even the closest magnetars (~ 1 kpc), the maximum positional shift due to parallax would be ~ 1 mas, and hence < 0.2 mas yr $^{-1}$ over the baselines probed, if such a shift were mis-attributed to proper motion. This is typically a factor of ~ 10 or more lower than the proper motions measured (see Table 3).

4.5. Birth sites

For the six counterparts with proper motions identified in Section 4, we produce 100 realisations of their past trajectories by sampling from the proper motion uncertainties and plotting these vectors with lengths corresponding to (i) their characteristic age (from the McGill catalogue Olausen & Kaspi 2014, and references therein) and (ii) an age ten times older than this to account for the possibility of inaccurate characteristic ages. We note that characteristic ages are typically upper limits, but that they could be higher if \dot{P} was measured outside quiescence, when spin-down rates can vary significantly (e.g. Woods et al. 2002; Kaspi & Gavriil 2003; Mori et al. 2013). Since the influence of the Galactic potential is not expected to significantly affect the trajectory of natal neutron stars on timescales of less than ~ 10 Myr (Disberg et al. 2024), the linear propagation of past trajectories is expected to be reliable for our purposes. The results are shown in Figure 8.

SGR 1935 can be traced back, within a factor of a few of its characteristic age, to the geometric centre of SNR G57.2+08 as first demonstrated by Lyman et al. (2022). 1E 2259 also has a past trajectory which passes close to the centre of a SNR (CTB

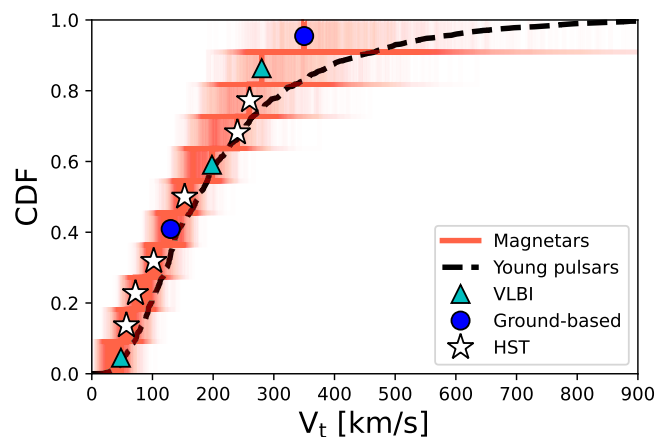


Fig. 7. The peculiar transverse velocity distribution of all magnetars with a velocity measurement (i.e. transverse velocities after correction for an assumed distance and hence local standard standard of rest). Each step in the distribution is labelled according to the method used to obtain the best available proper motion. One thousand random samples of the velocities, within their uncertainties (including distance uncertainty, see Table 3), are shown in red. Also shown is the transverse velocity distribution of pulsars with age < 10 Myr (the fiducial distribution of Disberg & Mandel 2025), which has been projected into 2D, assuming isotropy.

109, Fahlman & Gregory 1981; Tendulkar et al. 2013), but the magnetar must be significantly younger than its characteristic age which otherwise places the birth site well outside the SNR. As first shown by Chrimes et al. (2025), the direction and magnitude of SGR 0501's proper motion rules out an origin in the nearby SNR HB9, and no other plausible birth site has yet been identified. Similarly, no candidate SNR or stellar cluster has been found along the past trajectory of 4U 1042 (see also Tendulkar et al. 2013). SNR G127.1+0.5 lies within 2 deg of 4U 1042, but in the opposite direction. The past trajectory of PSR J1622 is

Table 3. Peculiar proper motions for the six NIR counterparts (re-)identified in this work. The proper motions of PSRJ1622 and 1RXSJ1708 are newly reported, previous measurements for the other four are provided in Table A.1 of the appendix. Also listed are the distances assumed for the six magnetars with NIR counterparts/candidates reported in this work, and the resulting peculiar transverse velocities this implies given the proper motion. Uncertainties on the v_t velocities do not include uncertainties on the distance, while the final column lists velocities $v_{t,d}$ which also include the quoted distance uncertainties (a 20% distance uncertainty is adopted for PSRJ 1622).

Magnetar	$\mu_\alpha \cos(\delta)$ [mas yr ⁻¹]	μ_δ [mas yr ⁻¹]	d [kpc]	Distance ref.	v_t [km/s]	$v_{t,d}$ [km/s]
PSRJ1622	9.7±7.1	1.6±5.8	~5	Yao et al. (2017)*	260±180	260 ⁺¹⁹⁸ ₋₁₉₂
1E 2259	-9.2±0.8	-4.0±0.2	3.2±0.2	Kothes & Foster (2012)	153±11	153±14
4U 0142	-5.5±0.5	2.2±0.2	3.6±0.4	Durant & van Kerkwijk (2006a)	102±9	102±15
SGR 0501	4.4±0.4	-4.0±0.5	2±1	Lin et al. (2011)	57±4	57±31
SGR 1935	-0.3±0.4	2.3±0.7	6.6±0.7†	Zhou et al. (2020)	72±20	72±21
1RXSJ 1708	-13±2	2.0±1.5	3.8±0.5	Durant & van Kerkwijk (2006a)	240±40	240±50

* - See also Section 4.3.1. † - See also Bailes et al. (2021).

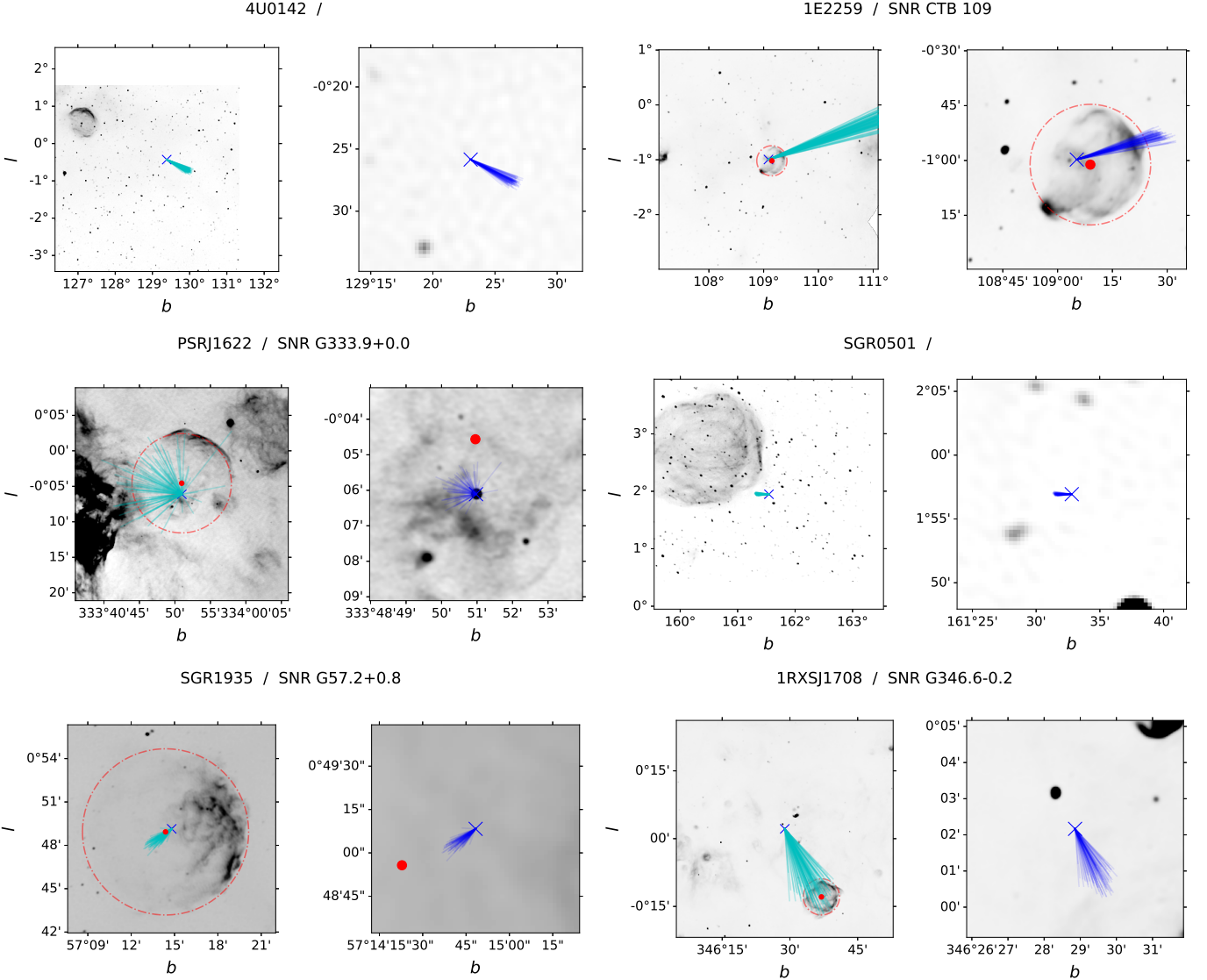


Fig. 8. The past trajectories of the magnetars for which we have measured a new/improved proper motion in this work. In each case we randomly sample 100 $(\mu_\alpha \cos(\delta), \mu_\delta)$ pairs from the measured proper motions and their uncertainties, assuming they are Gaussian. The lengths of the past trajectory vectors correspond to (i) 10 times the characteristic age, in cyan, and (ii) characteristic ages, in blue. The radial extent of the SNRs associated with 1E 2259, PSRJ1622, SGR 1935 and 1RXSJ 1708 are indicated with dashed red lines, and the approximate centres are marked with a red dot. The background radio images are from the 1.4 GHz Canadian Galactic Plane Survey (4U 0412, 1E 2259 and SGR 0501, Taylor et al. 2003) and the MeerKAT 1.3 GHz Galactic Plane Survey (PSRJ 1622, SGR 1935 and 1RXSJ 1708, Goedhart et al. 2024).

consistent, within a factor of ~ 2 of its characteristic age, with the centre of SNR G333.9+0.0 (first noted as a possible origin of this magnetar by Anderson et al. 2012).

Finally, the past trajectory of the object we claim to be the counterpart of 1RXS J1708 intersects SNR G346.6-0.2. There is no other neutron star association with this SNR (Green 2025). 1RXS J1708 would have to be ~ 10 times its characteristic age in order for this association to hold, although such a large kinematic age is not unprecedented - XTEJ1810 would have to be ~ 70 kyr old to be associated with SNR G11.0-0.0 (Helfand et al. 2007; Ding et al. 2020), and similar discrepancies have been seen in pulsars (e.g. Espinoza et al. 2022). Despite the past spatial coincidences, the reliability of these associations is called into question by the large discrepancies between the SNR and kinematic ages. Furthermore, distance estimates for SNR G346.6-0.2 are in the range ~ 5.5 -11 kpc (Koralesky et al. 1998; Sano et al. 2021), higher than the estimate of 3.8 ± 0.5 claimed for 1RXS J1708 based on red clump stars along that sight-line (Durant & van Kerkwijk 2006a). The F160W ($\sim H$ -band) absolute magnitude of the counterpart assuming 3.8 kpc and $A_V = 7.6$ would be ~ 5 , similar to known counterparts (Chrimes et al. 2022a). Placing it any further (up to the other extreme of 11 kpc) and behind higher extinction (up to the total Galactic extinction on that sight-line of $A_V \sim 60$, Schlafly & Finkbeiner 2011) pushes the source towards being intrinsically luminous and blue, inconsistent with known magnetar counterparts. It could feasibly then be a massive star, but given the co-location with the X-ray source, would presumably have to be a non-interacting companion to the magnetar, where the binary has been given a large natal kick without being unbound. The SNR has an estimated age of ~ 12 -14 kyr (assuming $d = 8 - 9$ kpc), and this would only decrease if placed at a lower distance (Auchettl et al. 2017; Sano et al. 2021). We proceed under the assumption that the SNR is at the lower end of the distance estimates, and that 1RXS J1708 was born in this supernova, but acknowledge the significant uncertainties in this interpretation.

5. Discussion

5.1. Magnetar natal kicks

The magnetar and young pulsar velocity distributions shown in Figure 7 appear similar, with a possible dearth of magnetars at the high velocity end. We carry out Anderson-Darling tests between 1000 realisations of the magnetar distribution, sampling from their proper motion uncertainties, and the transverse velocity distribution of young pulsars (Disberg & Mandel 2025). To avoid negative v_t values we perform log-normal sampling of the velocities. P-values > 0.05 are found in only 3% of the realisations. This formally rejects the null hypothesis that the magnetar velocities are drawn from the same underlying distribution as pulsars. The 16th, 50th and 84th percentiles of the magnetar velocity distributions yield $v_t = 154^{+141}_{-86}$ km s $^{-1}$. We repeat the process, each time removing the fastest 1% of the young pulsar distribution. We reach 5% of realisations with $p > 0.05$ once the fastest $\sim 15\%$ of pulsars have been removed. Similar to Ding et al. (2024), we therefore conclude that there is tentative evidence for a difference between the distributions, although this tension could plausibly be lessened by magnetar distance revisions. For example, we find that any distance revisions which gives just two magnetars in the sample a velocity of > 500 km s $^{-1}$ would be sufficient for the samples to become statistically indistinguishable.

Given our selection criteria, slow-moving magnetars which are not particularly red or variable (or happen to have similar magnitudes in the relevant epochs) may have been missed. Our selection may therefore be biased towards faster moving objects. For example, the source in the error circle of Swift J1834 appears to be moving against the bulk motion of objects in the field (Figure 4). However, its displacement across the 5 year baseline is only $\sim 2\sigma$ outside the scatter of all sources in the field. Given that the source is also not anomalous in colour and variability, we cannot yet confidently claim it as the counterpart. Further imaging on longer temporal baselines could determine whether this source truly has a discrepant proper motion for its field.

Conversely, for high proper motions > 15 mas yr $^{-1}$, over baselines of > 5 years, the object could have moved sufficiently that it is not recognised as the same object. This is because we use a matching radius of 75 mas to identify the same sources between different images. Similarly, objects could have moved outside the X-ray error circle, as these are static and typically from several years prior to the first HST observations (Olausen & Kaspi 2014). This is a potential bias against the detection of very high velocity objects. To investigate, we visually inspect the images of every magnetar, blinking the images between epochs to check for high proper motions and/or objects leaving the X-ray error circle. This is effective because large changes in position are obvious by eye (e.g. the motion of 1RXSJ 1708, with $\mu \sim 13$ mas yr $^{-1}$, is clearly visible when the images are blinked). We find no high-proper motion objects in the vicinity of the magnetar X-ray localisations, aside from those already identified as counterparts with the default selection criteria. We therefore conclude that a potential selection bias against very high v_t objects has not played a role in this sample.

5.2. Kinematic versus characteristic ages

For the sample of 11 magnetars with proper motion measurements, we collate information about their characteristic (P/\dot{P} spin-down) age τ_c in Table 4. Spin-down ages assume a braking index $n = 3$ (e.g. Hamil et al. 2015), that the magnetic field is dipolar and constant, and that $P_{\text{init}} \ll P$. These assumptions may not hold, particularly for magnetars, where the excess luminosity above that expected from spin-down is attributed to the decay of the magnetic field (Thompson & Duncan 1995). Therefore, τ_c may be an unreliable age indicator, and is an upper limit unless there are $P-\dot{P}$ variations due to variability during outbursts (Kaspi & Gavriil 2003; Mori et al. 2013).

We also list in Table 4 the angular offset to any SNR or stellar cluster association, where available, and report a kinematic age τ_k . The kinematic age uncertainties are propagated solely from the uncertainty on the proper motion, the uncertainty on the point of origin within the SNR or cluster is not quantified. Kinematic ages offers an independent constraint. They are defined as the time it would have taken, given the observed proper motion, to have travelled from the (estimated centroid of the) birth site to the current position. We further list the ages of associated SNRs in Table 4, where available.

In the left-hand panel of Figure 9, we plot τ_c versus τ_k for each case where a birth site has been identified. In every case the discrepancy is in the direction of the spin-down age underestimating the true age, with the exception of 1E 2259. The mean shift (excluding 1E 2259) is a factor of 4 ± 1 increase over the characteristic age. In general, characteristic ages are not reliable because magnetar spin-down rates are known to vary, the magnetic field is not constant, and is known not to be a simple dipole (e.g. Esposito et al. 2009). Kinematic ages are therefore

Table 4. Characteristic ages τ_c (from the McGill catalogue and references therein Olausen & Kaspi 2014), birth sites, and the approximate angular offsets to (the centre of) the proposed birth site. The six above the horizontal line have a HST derived proper motion; no birth site has been found for SGR 0501 and 4U 0142. Kinematic ages τ_k are listed for the remaining 5 magnetars with a proper motion constraint and candidate birth site (see Section 4.4 and Figure 7). All values are approximate, as we cannot determine the precise place of origin in a cluster, or the exact centre of a SNR remnant (due to non-symmetric expansion). The final columns list supernova remnant ages τ_{SN} (based on the size) where available, and their references.

Magnetar	τ_c [kyr]	Birth site	Birth site ref(s).	Ang. sep. [arcmin]	τ_k [kyr]	τ_{SN} [kyr]	τ_{SN} ref.
PSRJ1622	4	SNR G333.9+0.0	Anderson et al. (2012)	1.5	8 ± 6	< 6	Levin et al. (2010)
1E 2259	230	SNR CTB 109	(Tendulkar et al. 2013)	3	24 ± 2	12.7 ± 0.8	Leahy et al. (2020)
4U 0142	68	?	(Tendulkar et al. 2013)	-	-	-	-
SGR 0501	15	?	(Chrimes et al. 2025)	-	-	-	-
SGR 1935	3.6	SNR G57.2+0.8	Lyman et al. (2022)	0.6	16 ± 4	≥ 16	Zhou et al. (2020)
1RXSJ 1708 †	9	SNR G346.6-0.2	This work	20	90 ± 15	14 ± 2	Sano et al. (2021)
1E 1547	0.69	SNR G327.24-0.13	Camilo et al. (2007)	0.5	3 ± 1	-	-
SGR 1806	0.24	Stellar cluster	Tendulkar et al. (2012)	0.07	0.65 ± 0.19	-	-
SGR 1900	0.9	Stellar cluster	Tendulkar et al. (2012)	0.33	6 ± 1	-	-
XTE J1810 †	11	SNR G11.0-0.0	(Helfand et al. 2007)	19	70_{-10}^{+8}	$\lesssim 3$	Ding et al. (2020)
Swift J1818	0.24	SNR	Ibrahim et al. (2023)	0.2★	$1.20_{-1.15}^{+0.40}$	-	-

★ - judged by eye from Fig. 7 of Ibrahim et al. (2023). † - these magnetar-SNR associations should be treated with caution due to the large discrepancy between the characteristic/kinematic ages, and the SNR age.

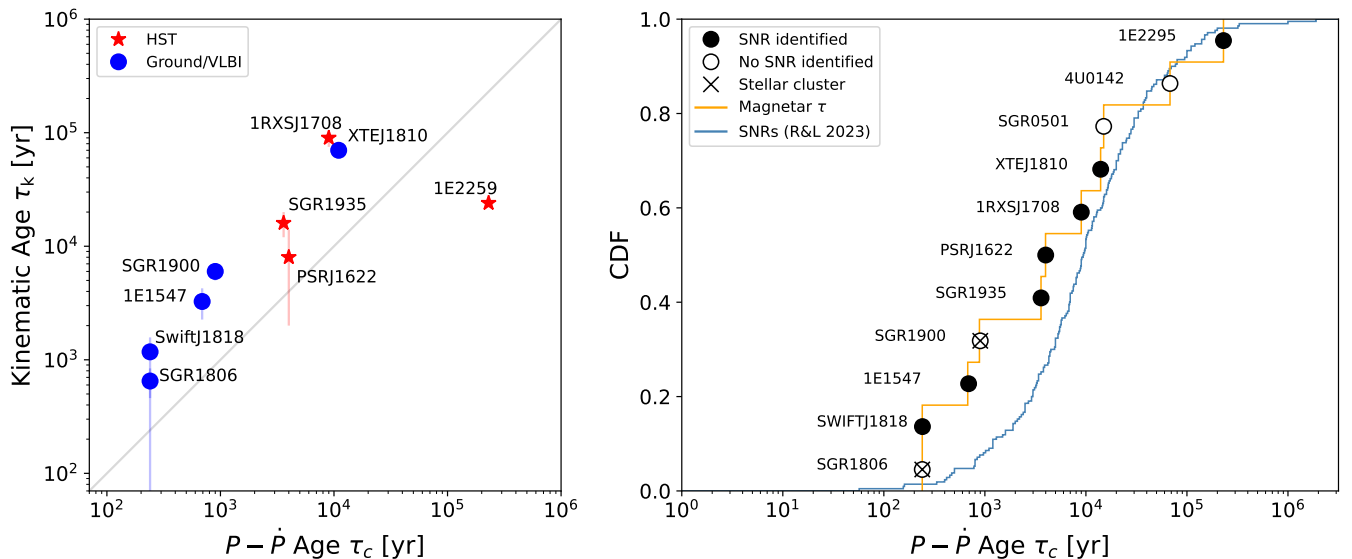


Fig. 9. Left panel: kinematic versus characteristic (spin-down) ages, for the subset of nine magnetars which have (i) a proper motion measurement and (ii) a SNR or stellar cluster along on the past trajectory (see Table 4). The characteristic ages τ_c are upper limits. The kinematic ages τ_k assume an origin in the approximate centre of the associated SNR or cluster, and their uncertainties are propagated solely from the uncertainty on the proper motion. The SNR associations for XTEJ1810 and 1RXSJ1708 should be treated with particular caution due to the large discrepancy between the characteristic/SNR ages and the kinematic ages. Right panel: the cumulative distribution of characteristic ages for the 11 magnetars which have a proper motion measurement (not including the Galactic centre object SGR 1745). Each object is labelled according to whether it has a SNR/stellar cluster association or no candidate birth site. Also shown is the cumulative distribution of Galactic SNR ages (Ranasinghe & Leahy 2023).

an independent way to determine magnetar and SNR ages simultaneously, ultimately constraining the physics governing the spin-down evolution of magnetars (e.g. Tendulkar et al. 2012; Li et al. 2026). However, the kinematic ages are more uncertain than listed in Table 4 and shown in Figure 9, where the uncertainties are propagated solely from the proper motion uncertainties. In addition to this, there are the uncertainties of (i) where in the SNR or cluster the magnetar originated, which may not necessarily be the geometric centre as assumed and (ii) the reliability of the birth site association - we may be incorrectly assigning the birth site. In at least two cases (1RXSJ1708 and XTE J1810),

there is a large discrepancy between the SNR age and kinematic age, which is challenging to explain and calls these associations into question. Furthermore, SGR 1900 and SGR 1806 have cluster associations, and there is a known bias against SNR detections in clusters (see the next subsection). Therefore, the true birth site may be closer than the cluster centroids assumed for the kinematic ages. If we assume that these four objects have spurious kinematic ages and remove them from Figure 9, the mean shift reduces to a factor of 3 ± 1 , and the significance of the result is further reduced when the uncertainty in the point of origin within the SNR is considered (e.g. SGR 1935 need not have orig-

inated at the geometric centre of SNR G57.2+08). On the other hand, if the SNRs associated with magnetar formation have already faded, given the distribution of SNR ages (Figure 9), this might also suggest a true age which is larger than the characteristic age. To quantify these uncertainties, a detailed study of the observational biases at different wavelengths, the probability of chance alignments, and the evolution of SNRs throughout the Galactic plane would be needed.

If the result suggested by Figure 9 were to hold, it would imply fewer young neutron stars in the Galaxy than suggested by their characteristic ages, which has implications for their birth rates and the fraction of neutron stars which are born as magnetars (Beniamini et al. 2019; Jawor & Tauris 2022; Sautron et al. 2025; Pardo-Araujo et al. 2026). For example, in this sample, increasing the characteristic ages by a factor of three reduces the number of magnetars younger than 2 kyr by a factor of 2 and those younger than 20 kyr by a factor of 1.3. This would imply a corresponding reduction in the fraction of neutron stars born as magnetars, a reduction in the completeness of the Galactic magnetar sample, or some combination thereof. However, we stress again that these conclusions depend entirely on both the counterpart and birth site associations being robust.

5.3. Magnetars without SNR associations

A parent SNR or stellar cluster has not been identified in every case. We ask whether this is surprising, given the age of the magnetar, and assuming that the characteristic age is representative (within some scatter as described above). In the right hand panel of Figure 9, we plot the cumulative distribution of τ_c for the 11 magnetars with a proper motion and hence an opportunity to determine the birth site. Each step in the distribution is labelled by the magnetar name and whether a SNR association has been made. Also shown is the age distribution of Galactic SNRs (Ranasinghe & Leahy 2023). All 11 magnetars lie in the same age range as Galactic SNRs, and 7 have at least a tentatively associated SNR which is consistent with the past trajectory. Although not included here due to the likely influence of Sgr A* on its motion, SGR 1745 has also been linked with a SNR (Ponti et al. 2015; Yalinewich et al. 2017).

A further two (SGR 1900 and SGR 1806) are not associated with a SNR, these both have ages at the lower end of the Galactic SNR age distribution. They are, however, linked with massive stellar clusters (Tendulkar et al. 2012), and there are known biases against SNR detection in clusters due to the merging of individual remnants in dense environments (e.g. Vasiliev et al. 2017), confusion with the diffuse background/HII region emission (Anderson et al. 2017, 2025; ?) and the small angular sizes of young SNRs in dense environments (Verberne & Vink 2021).

Finally, SGR 0501 and 4U 0142 are the only two magnetars with a well constrained past trajectory but no obvious SNR or parent stellar cluster. They are among the oldest objects in the sample, but SNRs with similar ages are known. If the SNR HB9 were the origin of SGR 0501 (neglecting for a moment the direction of the proper motion vector), the kinematic age would be $\sim 10^6$ years, in the extreme tail of the SNR age distribution. Given the spin-down age of ~ 15 kyr, this would be by far the largest discrepancy in the left panel of Figure 9. Although we show characteristic ages in the right panel of Figure 9, the true (kinematic) age of 1E 2259 is a factor of ~ 10 younger, so the detection of the associated SNR is consistent known SNR ages, in contrast with the 4U 0142 and SGR 0501 non-detections. If the association of 1RXSJ 1708 with SNR G346.6-0.2 holds, it must

be a factor of ~ 10 older than the characteristic age, which would also make SNR G346.6-0.2 one of the oldest SNRs known.

Crucially, in the other cases where no SNR was identified (SGR 1900 and SGR 1806), massive star clusters were nevertheless present. Given that the lifetimes of even massive stars are at least 2 orders of magnitude longer than the ages of SGR0501 and 4U0142, and their positions in the Galactic anti-centre direction with relatively low extinction on their sight-lines, the lack of massive stars/clusters along their past trajectories is also surprising. Non-core-collapse channels such as accretion induced collapse (Nomoto & Kondo 1991) and low-mass neutron star mergers (Giacomazzo & Perna 2013; Piro et al. 2017) are challenged by the low Galactic latitudes of SGR 0501 and 4U 0412 which should not necessarily be favoured by these formation pathways. Another possible explanation may be that their progenitor stars were ejected from their parent clusters, either by the supernova of a companion (e.g. Blaauw 1961; Renzo et al. 2019) or dynamical interactions (e.g. Poveda et al. 1967; de Wit et al. 2005). Massive runaway stars could travel hundreds or even thousands of parsecs in such a scenario before going supernova (e.g. Eldridge et al. 2011).

6. Conclusions

In this paper, we searched for NIR counterparts to Galactic magnetars in repeat HST (and in one case single-epoch JWST) imaging. We re-discovered the counterparts of four magnetars (4U 1042, 1E 2259, SGR 0501, SGR 1935), reducing the uncertainties on their proper motions, and report new candidates for a further three (PSR J1622, 1RXSJ 1708, CXOUJ 1647), measuring the first proper motions for PSR J 1622 and 1RXSJ 1708. We find that magnetar characteristic ages may be underestimates of their true ages, based on SNR and stellar cluster associations. However, this results hinges on the reliability of these birth site associations.

We show that magnetar transverse velocities and birth sites are broadly similar to that of young pulsars, with the notable exceptions of SGR 0501 and 4U 0142 for which no candidate birth sites have yet been identified. This is consistent with the idea that magnetars evolve into other classes of neutron star such as X-ray dim isolated neutron stars (e.g. Borghese & Esposito 2023; Gençali & Ertan 2024), and searches for companion stars (Chrimes et al. 2022a), which broadly match expectations for neutron stars in general. However, there is some evidence (Sherman et al. 2024) that magnetars may be preferentially formed in the core-collapse of merger products based on a lack of unbound companions (see also Tendulkar et al. 2012; Schneider et al. 2019, 2020; Shenar et al. 2023). We also show that tentative evidence is emerging for a dearth of high-velocity magnetars, compared with young pulsars. If real, this effect may arise from an as yet unidentified physical preference in the progenitor population which produces magnetars, and/or some difference in their post-formation velocity evolution.

The faintness of the new counterparts we have identified in this work (>23.5 AB at $1.6\mu\text{m}$), coupled with crowded sight-lines through the Galactic plane, demonstrates the strength of sensitive, high spatial resolution NIR observations for multi-wavelength neutron star studies. We have also shown that, while effective, magnetar counterpart selection based on colour, variability and proper motion may miss some objects and could be biased towards higher transverse velocities. For example, the discovery of the counterpart of CXOUJ1647 required a JWST spectral energy distribution. Future multi-filter and multi-epoch JWST studies will enable redder, fainter and higher spatial res-

olution observations. The constraints achievable depend on the signal-to-noise (S/N) ratio of the source, but for targets detected with $S/N=20$, we estimate that with observing baselines of 3 years, NIRcam observations can probe proper motions as small as 1 mas yr^{-1} . At this level, parallaxes may even be measurable for nearby magnetars if the observations are coordinated carefully (previously only possible for neutron stars within $\sim 100 \text{ pc}$, Walter & Lattimer 2002). There are a range of potential applications, not only to magnetars, but any faint objects in the Galactic plane and Galactic centre for which kinematics are scientifically interesting (e.g. Libralato et al. 2023).

Acknowledgements. The authors thank Nanda Rea for insightful discussions. AAC and AB acknowledge support through the European Space Agency (ESA) research fellowship programme. JDL acknowledges support from a UK Research and Innovation Fellowship (MR/T020784/1). NRT is supported by STFC Consolidated grant ST/W000857/1.

This research is based on observations made with the NASA/ESA Hubble Space Telescope obtained from the Space Telescope Science Institute, which is operated by the Association of Universities for Research in Astronomy, Inc., under NASA contract NAS 5–26555. These observations are associated with program 17927. This work is based in part on observations made with the NASA/ESA/CSA James Webb Space Telescope. The data were obtained from the Mikulski Archive for Space Telescopes at the Space Telescope Science Institute, which is operated by the Association of Universities for Research in Astronomy, Inc., under NASA contract NAS 5-03127 for JWST. These observations are associated with program GO 1905. This work made use of data from the European Space Agency (ESA) mission *Gaia* ([https://www.cosmos.esa.int/{\protect\relax\itshapeGaia}](https://www.cosmos.esa.int/{\protect\relax\itshapeGaia}})), processed by the *Gaia* Data Processing and Analysis Consortium (DPAC, <https://www.cosmos.esa.int/web/{\protect\relax\itshapeGaia}/dpac/consortium>). Funding for the DPAC has been provided by national institutions, in particular the institutions participating in the *Gaia* Multilateral Agreement.

We acknowledge use of the McGill magnetar (Olausen & Kaspi 2014), Green (Green 2025), and University of Manitoba SNRcat (Ferrand & Safi-Harb 2012)⁶ supernova remnant catalogues. This research has made use of the SVO Filter Profile Service “Carlos Rodrigo”, funded by MCIN/AEI/10.13039/501100011033/ through grant PID2023-146210NB-I00 (Rodrigo et al. 2012; Rodrigo & Solano 2020; Rodrigo et al. 2024). This work made use of `IPYTHON` (Perez & Granger 2007), `NUMPY` (Harris et al. 2020), `SCIPY` (Virtanen et al. 2020), `MATPLOTLIB` (Hunter 2007), and `ASTROPY` (<https://www.astropy.org>), a community-developed core Python package for Astronomy (Astropy Collaboration et al. 2013; Price-Whelan et al. 2018). We have also made use of the python modules `DUSTMAPS` (Green 2018) and `EXTINCTION` (Barbary 2016).

References

Anderson, G. E., Gaensler, B. M., Slane, P. O., et al. 2012, *ApJ*, 751, 53
 Anderson, J. 2016, Empirical Models for the WFC3/IR PSF, Instrument Science Report WFC3 2016-12, 42 pages
 Anderson, L. D., Camilo, F., Faerber, T., et al. 2025, *A&A*, 693, A247
 Anderson, L. D., Wang, Y., Bihl, S., et al. 2017, *A&A*, 605, A58
 Astropy Collaboration, Robitaille, T. P., Tollerud, E. J., et al. 2013, *A&A*, 558, A33
 Auchettl, K., Ng, C.-Y., Wong, B. T. T., Lopez, L., & Slane, P. 2017, *ApJ*, 847, 121
 Bailes, M., Bassa, C. G., Bernardi, G., et al. 2021, *MNRAS*, 503, 5367
 Barbary, K. 2016, *extinction* v0.3.0
 Bedin, L. R. & Fontanive, C. 2018, *MNRAS*, 481, 5339
 Beniamini, P., Hotokezaka, K., van der Horst, A., & Kouveliotou, C. 2019, *MNRAS*, 487, 1426
 Blaauw, A. 1961, *Bull. Astron. Inst. Netherlands*, 15, 265
 Bochenek, C. D., Ravi, V., Belov, K. V., et al. 2020, *Nature*, 587, 59
 Borghese, A. & Esposito, P. 2023, in *Handbook of X-ray and Gamma-ray Astrophysics*, 146
 Bower, G. C., Deller, A., Demorest, P., et al. 2015, *ApJ*, 798, 120
 Burns, E., Svinikin, D., Hurley, K., et al. 2021, *ApJ*, 907, L28
 Camilo, F., Ransom, S. M., Halpern, J. P., & Reynolds, J. 2007, *ApJ*, 666, L93
 Camilo, F., Ransom, S. M., Halpern, J. P., et al. 2006, *Nature*, 442, 892
 Camilo, F., Reynolds, J., Johnston, S., Halpern, J. P., & Ransom, S. M. 2008, *ApJ*, 679, 681

CHIME/FRB Collaboration, Andersen, B. C., Bandura, K. M., et al. 2020, *Nature*, 587, 54
 Chrimes, A. A., Levan, A. J., Fruchter, A. S., et al. 2022a, *MNRAS*, 513, 3550
 Chrimes, A. A., Levan, A. J., Fruchter, A. S., et al. 2022b, *MNRAS*, 512, 6093
 Chrimes, A. A., Levan, A. J., Lyman, J. D., et al. 2025, *A&A*, 696, A127
 Clark, J. S., Ritchie, B. W., Najarro, F., Langer, N., & Negueruela, I. 2014, *A&A*, 565, A90
 Cordes, J. M. & Lazio, T. J. W. 2002, arXiv e-prints, astro
 Coti Zelati, F., Rea, N., Pons, J. A., Campana, S., & Esposito, P. 2018, *MNRAS*, 474, 961
 Davies, B., Figer, D. F., Kudritzki, R.-P., et al. 2009, *ApJ*, 707, 844
 de Wit, W. J., Testi, L., Palla, F., & Zinnecker, H. 2005, *A&A*, 437, 247
 Deller, A. T., Camilo, F., Reynolds, J. E., & Halpern, J. P. 2012, *ApJ*, 748, L1
 Dhillon, V. S., Marsh, T. R., Hulleman, F., et al. 2005, *MNRAS*, 363, 609
 Dhillon, V. S., Marsh, T. R., Littlefair, S. P., et al. 2011, *MNRAS*, 416, L16
 Ding, H., Deller, A. T., Lower, M. E., et al. 2020, *MNRAS*, 498, 3736
 Ding, H., Lower, M. E., Deller, A. T., et al. 2024, *ApJ*, 971, L13
 Ding, P.-J., Zhu, Z., & Liu, J.-C. 2019, *Research in Astronomy and Astrophysics*, 19, 068
 Disberg, P., Gaspari, N., & Levan, A. J. 2024, *A&A*, 687, A272
 Disberg, P. & Mandel, I. 2025, *ApJ*, 989, L8
 Dolphin, A. 2016, DOLPHOT: Stellar photometry, *Astrophysics Source Code Library*, record ascl:1608.013
 Dolphin, A. E. 2000, *PASP*, 112, 1383
 Durant, M. & van Kerkwijk, M. H. 2005, *ApJ*, 627, 376
 Durant, M. & van Kerkwijk, M. H. 2006a, *ApJ*, 650, 1070
 Durant, M. & van Kerkwijk, M. H. 2006b, *ApJ*, 652, 576
 Durant, M. & van Kerkwijk, M. H. 2006c, *ApJ*, 648, 534
 Eikenberry, S. S., Matthews, K., LaVine, J. L., et al. 2004, *ApJ*, 616, 506
 Eldridge, J. J., Langer, N., & Tout, C. A. 2011, *MNRAS*, 414, 3501
 Ertan, Ü., Erkut, M. H., Ekşi, K. Y., & Alpar, M. A. 2007, *ApJ*, 657, 441
 Espinoza, C. M., Vidal-Navarro, M., Ho, W. C. G., Deller, A., & Chatterjee, S. 2022, *A&A*, 659, A41
 Esposito, P., Burgay, M., Possenti, A., et al. 2009, *MNRAS*, 399, L44
 Esposito, P., Rea, N., Borghese, A., et al. 2020, *ApJ*, 896, L30
 Esposito, P., Rea, N., & Israel, G. L. 2021, in *Astrophysics and Space Science Library*, Vol. 461, *Timing Neutron Stars: Pulsations, Oscillations and Explosions*, ed. T. M. Belloni, M. Méndez, & C. Zhang, 97–142
 Fahlman, G. G. & Gregory, P. C. 1981, *Nature*, 293, 202
 Ferrand, G. & Safi-Harb, S. 2012, *Advances in Space Research*, 49, 1313
 Ferrario, L. & Wickramasinghe, D. 2006, *MNRAS*, 367, 1323
 Fitzpatrick, E. L. 1999, *PASP*, 111, 63
 Fruchter, A. S. & Hook, R. N. 2002, *PASP*, 114, 144
 Gaia Collaboration, Vallenari, A., Brown, A. G. A., et al. 2023, *A&A*, 674, A1
 Gelfand, J. D. & Gaensler, B. M. 2007, *ApJ*, 667, 1111
 Gençali, A. A. & Ertan, Ü. 2024, *MNRAS*, 534, 1481
 Giacomazzo, B. & Perna, R. 2013, *ApJ*, 771, L26
 Gilmozzi, R. & Spyromilio, J. 2007, *The Messenger*, 127, 11
 Goedhart, S., Cotton, W. D., Camilo, F., et al. 2024, *MNRAS*, 531, 649
 Gompertz, B. P., O’Brien, P. T., & Wynn, G. A. 2014, *MNRAS*, 438, 240
 Green, D. A. 2025, *Journal of Astrophysics and Astronomy*, 46, 14
 Green, G. M. 2018, *The Journal of Open Source Software*, 3, 695
 Guarcello, M. G., Almedros-Abad, V., Lovell, J. B., et al. 2025, *A&A*, 693, A120
 Hamil, O., Stone, J. R., Urbanec, M., & Urbanová, G. 2015, *Phys. Rev. D*, 91, 063007
 Hare, J., Pavlov, G. G., Posselt, B., et al. 2024, *ApJ*, 972, 176
 Harris, C. R., Millman, K. J., van der Walt, S. J., et al. 2020, *Nature*, 585, 357
 Helfand, D. J., Chatterjee, S., Briskin, W. F., et al. 2007, *ApJ*, 662, 1198
 Hobbs, G., Lorimer, D. R., Lyne, A. G., & Kramer, M. 2005, *MNRAS*, 360, 974
 Hu, R.-C. & Zhang, B. 2025, arXiv e-prints, arXiv:2511.06554
 Hulleman, F., Tennant, A. F., van Kerkwijk, M. H., et al. 2001, *ApJ*, 563, L49
 Hulleman, F., van Kerkwijk, M. H., & Kulkarni, S. R. 2004, *A&A*, 416, 1037
 Hunter, J. D. 2007, *Computing in Science and Engineering*, 9, 90
 Ibrahim, A. Y., Borghese, A., Rea, N., et al. 2023, *ApJ*, 943, 20
 Igoshev, A. P. 2020, *MNRAS*, 494, 3663
 Igoshev, A. P., Popov, S. B., & Hollerbach, R. 2021, *Universe*, 7, 351
 Israel, G., Covino, S., Mignani, R., et al. 2005, *A&A*, 438, L1
 Israel, G. L., Covino, S., Perna, R., et al. 2003, *ApJ*, 589, L93
 Israel, G. L., Covino, S., Stella, L., et al. 2002, *ApJ*, 580, L143
 Jawor, J. A. & Tauris, T. M. 2022, *MNRAS*, 509, 634
 Kaplan, D. L., Chatterjee, S., Hales, C. A., Gaensler, B. M., & Slane, P. O. 2009, *AJ*, 137, 354
 Kaspi, V. M. & Beloborodov, A. M. 2017, *ARA&A*, 55, 261
 Kaspi, V. M. & Gavriil, F. P. 2003, *ApJ*, 596, L71
 Kern, B. & Martin, C. 2002, *Nature*, 417, 527

⁶ <http://snrcat.physics.umanitoba.ca>

- Kimble, R. A., MacKenty, J. W., O'Connell, R. W., & Townsend, J. A. 2008, in *Society of Photo-Optical Instrumentation Engineers (SPIE) Conference Series*, Vol. 7010, *Space Telescopes and Instrumentation 2008: Optical, Infrared, and Millimeter*, ed. J. M. Oschmann, Jr., M. W. M. de Graauw, & H. A. MacEwen, 70101E
- Kirsten, F., Marcote, B., Nimmo, K., et al. 2022, *Nature*, 602, 585
- Koralesky, B., Frail, D. A., Goss, W. M., Claussen, M. J., & Green, A. J. 1998, *AJ*, 116, 1323
- Kosugi, G., Ogasawara, R., & Terada, H. 2005, *ApJ*, 623, L125
- Kothes, R. & Foster, T. 2012, *ApJ*, 746, L4
- Kouveliotou, C., Dieters, S., Strohmayer, T., et al. 1998, *Nature*, 393, 235
- Kouveliotou, C., Strohmayer, T., Hurley, K., et al. 1999, *ApJ*, 510, L115
- Leahy, D. A., Ranasinghe, S., & Gelowitz, M. 2020, *ApJS*, 248, 16
- Levan, A., Kouveliotou, C., & Fruchter, A. 2018, *ApJ*, 854, 161
- Levan, A. J., Wynn, G. A., Chapman, R., et al. 2006, *MNRAS*, 368, L1
- Levin, L., Bailes, M., Bates, S., et al. 2010, *ApJ*, 721, L33
- Li, B., Gao, Z., Ma, W., et al. 2026, arXiv e-prints, arXiv:2602.06615
- Libralato, M., Bellini, A., van der Marel, R. P., et al. 2023, *ApJ*, 950, 101
- Lin, L., Kouveliotou, C., Baring, M. G., et al. 2011, *ApJ*, 739, 87
- Lyman, J. D., Levan, A. J., Wiersema, K., et al. 2022, *ApJ*, 926, 121
- Margalit, B., Berger, E., & Metzger, B. D. 2019, *ApJ*, 886, 110
- Mazets, E. P., Golentskii, S. V., Ilinskii, V. N., Aptekar, R. L., & Guryan, I. A. 1979, *Nature*, 282, 587
- Mereghetti, S., Pons, J. A., & Melatos, A. 2015, *Space Sci. Rev.*, 191, 315
- Mereghetti, S., Rigoselli, M., Salvaterra, R., et al. 2024, *Nature*, 629, 58
- Metzger, B. D., Margalit, B., Kasen, D., & Quataert, E. 2015, *MNRAS*, 454, 3311
- Mori, K., Gotthelf, E. V., Zhang, S., et al. 2013, *ApJ*, 770, L23
- Morii, M., Kawai, N., Kataoka, J., et al. 2005, *Advances in Space Research*, 35, 1177
- Mösta, P., Ott, C. D., Radice, D., et al. 2015, *Nature*, 528, 376
- Muñoz-Darias, T., de Ugarte Postigo, A., & Casares, J. 2016, *MNRAS*, 458, L114
- Muno, M. P., Clark, J. S., Crowther, P. A., et al. 2006, *ApJ*, 636, L41
- Negro, M., Younes, G., Wadiasingh, Z., et al. 2024, *Frontiers in Astronomy and Space Sciences*, 11, 1388953
- Nomoto, K. & Kondo, Y. 1991, *ApJ*, 367, L19
- Obergaulinger, M., Janka, H. T., & Aloy, M. A. 2014, *MNRAS*, 445, 3169
- Oke, J. B. & Gunn, J. E. 1983, *ApJ*, 266, 713
- Olausen, S. A. & Kaspi, V. M. 2014, *ApJS*, 212, 6
- Omand, C. M. B. & Sarin, N. 2024, *MNRAS*, 527, 6455
- Palmer, D. M., Barthelmy, S., Gehrels, N., et al. 2005, *Nature*, 434, 1107
- Pardo-Araujo, C., Rea, N., Ronchi, M., & Graber, V. 2026, arXiv e-prints, arXiv:2601.16159
- Penoyre, Z., Belokurov, V., & Evans, N. W. 2022, *MNRAS*, 513, 2437
- Perez, F. & Granger, B. E. 2007, *Computing in Science and Engineering*, 9, 21
- Piro, A. L., Giacomazzo, B., & Perna, R. 2017, *ApJ*, 844, L19
- Ponti, G., Morris, M. R., Terrier, R., et al. 2015, *MNRAS*, 453, 172
- Poveda, A., Ruiz, J., & Allen, C. 1967, *Boletín de los Observatorios Tonantzintla y Tacubaya*, 4, 86
- Predehl, P. & Schmitt, J. H. M. M. 1995, *A&A*, 293, 889
- Price-Whelan, A. M., Sipőcz, B. M., Günther, H. M., et al. 2018, *AJ*, 156, 123
- Ranasinghe, S. & Leahy, D. 2023, *ApJS*, 265, 53
- Rea, N., Gullón, M., Pons, J. A., et al. 2015, *ApJ*, 813, 92
- Reboul-Salze, A., Guilet, J., Raynaud, R., & Bugli, M. 2022, *A&A*, 667, A94
- Renzo, M., Zapartas, E., de Mink, S. E., et al. 2019, *A&A*, 624, A66
- Rigoselli, M., Mereghetti, S., Halpern, J. P., Gotthelf, E. V., & Bassa, C. G. 2024, *ApJ*, 976, 228
- Ritchie, B. W., Clark, J. S., Negueruela, I., & Langer, N. 2010, *A&A*, 520, A48
- Rodrigo, C., Cruz, P., Aguilar, J. F., et al. 2024, *A&A*, 689, A93
- Rodrigo, C. & Solano, E. 2020, in *XIV.0 Scientific Meeting (virtual) of the Spanish Astronomical Society*, 182
- Rodrigo, C., Solano, E., & Bayo, A. 2012, *SVO Filter Profile Service Version 1.0, IVOA Working Draft 15 October 2012*
- Sano, H., Suzuki, H., Nobukawa, K. K., et al. 2021, *ApJ*, 923, 15
- Sautron, M., McEwen, A. E., Younes, G., et al. 2025, *ApJ*, 986, 88
- Schlaflly, E. F. & Finkbeiner, D. P. 2011, *ApJ*, 737, 103
- Schneider, F. R. N., Ohlmann, S. T., Podsiadlowski, P., et al. 2020, *MNRAS*, 495, 2796
- Schneider, F. R. N., Ohlmann, S. T., Podsiadlowski, P., et al. 2019, *Nature*, 574, 211
- Shannon, R. M. & Johnston, S. 2013, *MNRAS*, 435, L29
- Sharma, K., Somalwar, J., Law, C., et al. 2023, *ApJ*, 950, 175
- Shenar, T., Wade, G. A., Marchant, P., et al. 2023, *Science*, 381, 761
- Sherman, M. B., Ravi, V., El-Badry, K., et al. 2024, *MNRAS*, 531, 2379
- Tam, C. R., Kaspi, V. M., van Kerkwijk, M. H., & Durant, M. 2004, *ApJ*, 617, L53
- Taylor, A. R., Gibson, S. J., Peracaula, M., et al. 2003, *AJ*, 125, 3145
- Tendulkar, S. P., Cameron, P. B., & Kulkarni, S. R. 2012, *ApJ*, 761, 76
- Tendulkar, S. P., Cameron, P. B., & Kulkarni, S. R. 2013, *ApJ*, 772, 31
- Testa, V., Mignani, R. P., Hummel, W., Rea, N., & Israel, G. L. 2018, *MNRAS*, 473, 3180
- Testa, V., Rea, N., Mignani, R. P., et al. 2008, *A&A*, 482, 607
- Thompson, C. & Duncan, R. C. 1993, *ApJ*, 408, 194
- Thompson, C. & Duncan, R. C. 1995, *MNRAS*, 275, 255
- Thompson, C. & Duncan, R. C. 1996, *ApJ*, 473, 322
- Turolla, R., Zane, S., & Watts, A. L. 2015, *Reports on Progress in Physics*, 78, 116901
- van Paradijs, J., Taam, R. E., & van den Heuvel, E. P. J. 1995, *A&A*, 299, L41
- Vasiliev, E. O., Shchekinov, Y. A., & Nath, B. B. 2017, *MNRAS*, 468, 2757
- Verberne, S. & Vink, J. 2021, *MNRAS*, 504, 1536
- Verbunt, F., Igoshev, A., & Cator, E. 2017, *A&A*, 608, A57
- Vink, J. & Kuiper, L. 2006, *MNRAS*, 370, L14
- Virtanen, P., Gommers, R., Oliphant, T. E., et al. 2020, *Nature Methods*, 17, 261
- Walter, F. M. & Lattimer, J. M. 2002, *ApJ*, 576, L145
- Wang, Z., Chakrabarty, D., & Kaplan, D. L. 2006, *Nature*, 440, 772
- Weisz, D. R., Dolphin, A. E., Savino, A., et al. 2024, *ApJS*, 271, 47
- White, C. J., Burrows, A., Coleman, M. S. B., & Vartanyan, D. 2022, *ApJ*, 926, 111
- Woltjer, L. 1964, *ApJ*, 140, 1309
- Woods, P. M., Kouveliotou, C., Göğüş, E., et al. 2002, *ApJ*, 576, 381
- Yalinewich, A., Piran, T., & Sari, R. 2017, *ApJ*, 838, 12
- Yao, J. M., Manchester, R. N., & Wang, N. 2017, *ApJ*, 835, 29
- Zhou, P., Zhou, X., Chen, Y., et al. 2020, *ApJ*, 905, 99

Appendix A: Additional information

In this appendix we provide,

- Table A.1, which lists previous proper motion and velocity information for the 11 magnetars in our velocity sample,
- Figure A.1 which shows the NIR light-curves for the six counterparts/candidates identified in HST imaging,
- Two figures (A.2 and A.3) showing our proper motion fits for the six magnetars with a *Hubble* proper motion measurement.

Table A.1. Proper motion, distance and transverse velocity information for the sample of 11 magnetars with these measurements as defined in Section 4.4. Above the horizontal line: an extension of Table 3 providing previous proper motion measurements, where available, for the six objects we have measured proper motions for in this work. Below the line: previously reported proper motion measurements, distance estimates and transverse velocities for the remaining five objects. Velocity uncertainties include the quoted distance uncertainty in each case.

Magnetar	$\mu_{\alpha,\text{prev}} \cos(\delta)$ [mas yr ⁻¹]	$\mu_{\delta,\text{prev}}$ [mas yr ⁻¹]	μ_{prev} ref		
PSRJ1622	-	-	-		
1E 2259	-9.9±1.1	-3.0±1.1	Tendulkar et al. (2013)		
4U 0142	-5.6±1.3	2.9±1.3	Tendulkar et al. (2013)		
SGR 0501	4.1±0.7	-3.5±0.4	Chrimes et al. (2025)		
SGR 1935	-0.7±0.8	3.1±1.6	Lyman et al. (2022)		
1RXSJ 1708	-	-	-		
Magnetar	$\mu_{\alpha,\text{prev}} \cos(\delta)$ [mas yr ⁻¹]	$\mu_{\delta,\text{prev}}$ [mas yr ⁻¹]	d [kpc]	$v_{t,\text{unc}}$ [km/s]	$\mu_{\text{prev}}, d + v_{t,d}$ ref.
1E 1547	4.8±0.5	-7.9±0.3	6±2	280 ⁺¹³⁰ ₋₁₂₀	Deller et al. (2012)
SGR 1806	4.2±0.9	7.0±1.8	9±2	350±100	Tendulkar et al. (2012)
SGR 1900	2.7±0.2	4.8±0.4	12.5±1.6	130±30	Tendulkar et al. (2012)
XTE J1810	-3.79 ^{+0.05} _{-0.03}	-16.2±0.1	2.5 ^{+0.4} _{-0.3}	198 ⁺²⁹ ₋₂₃	Ding et al. (2020)
Swift J1818	-3.57±0.02	-7.72±0.06	9.4 ^{+2.0} _{-1.4}	48 ⁺⁵⁰ ₋₁₆	Ding et al. (2024)

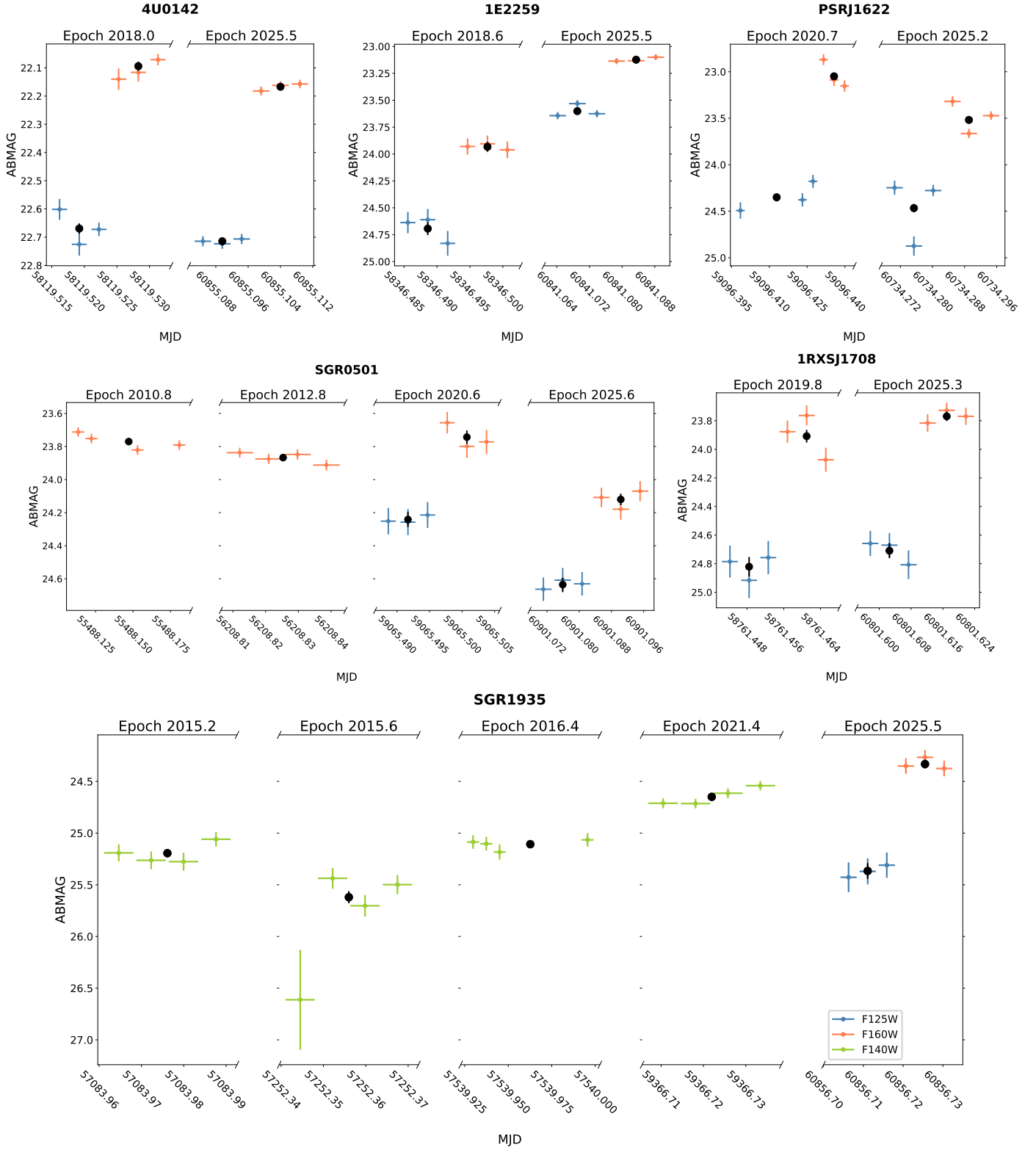


Fig. A.1. Near-IR HST $_{FLT}$ -level light-curves for the six counterparts identified in our sample. F125W apparent magnitudes are coloured blue, F160W (which are exclusively fainter than F125W) orange and F140W green (the first four epochs for SGR 1935 only). Note that each subplot has different y-axis limits. Values are reported in the AB system and are not corrected for Galactic extinction. In each epoch, photometry on the combined, drizzled $_{DRZ}$ image is also show as a black point with error-bars at the midpoint of the $_{FLT}$ observations.

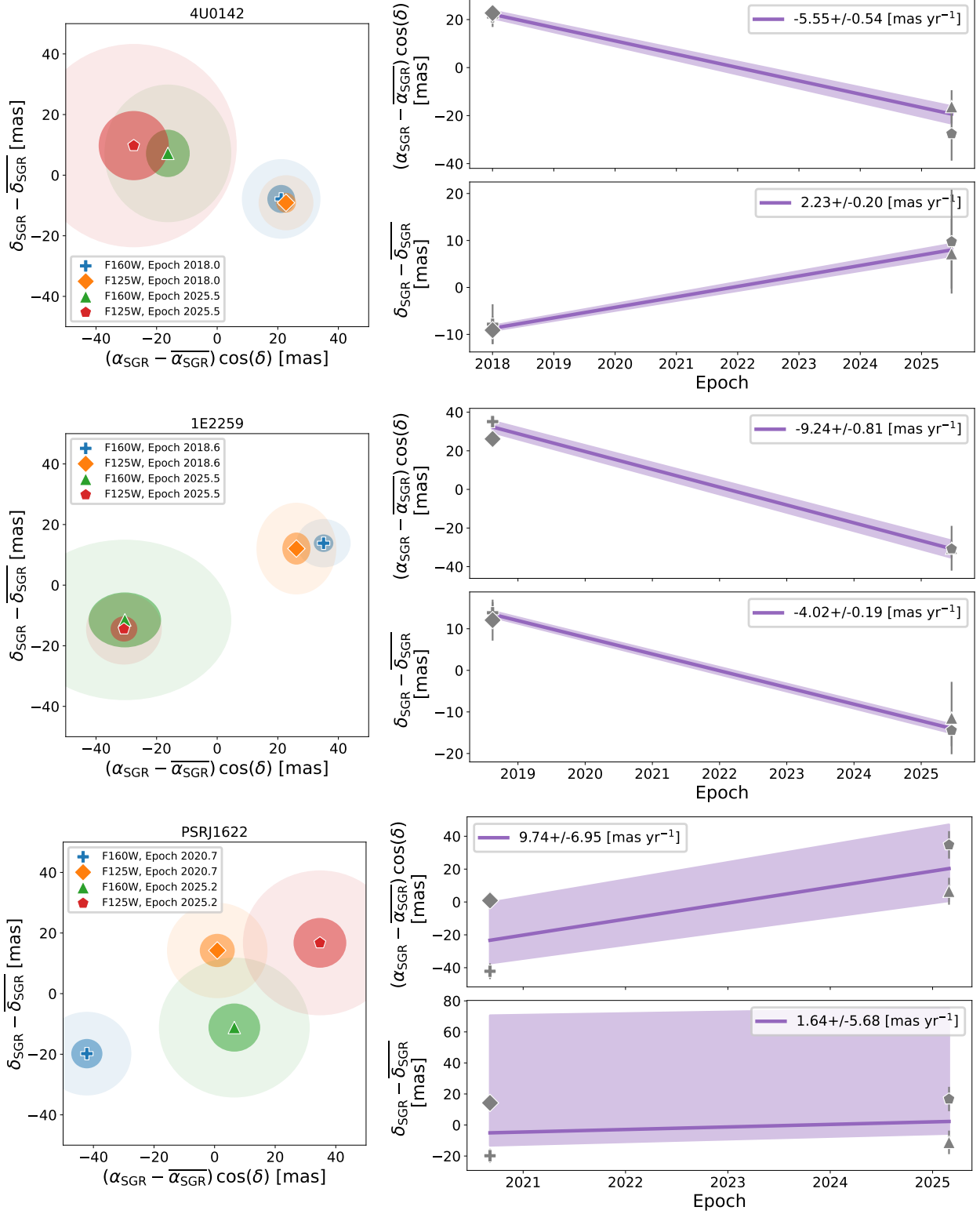


Fig. A.2. Proper motion measurements for 4U 1042, 1E 2259 and PSRJ 1622. Left panels: IR counterpart offsets in α, δ with respect to the mean position across the four epochs, and the 1σ (dark shading) and 3σ (lighter shading) uncertainties on these offsets. Right panels: peculiar proper motions determined from each epoch and the best fit to all four measurements. The symbols match the epochs/filters shown in the left-hand panel. The proper motion in declination is poorly constrained for PSRJ1622, and could also be expressed as an upper limit on the proper motion of $\mu_\delta < 11.2 \text{ mas yr}^{-1}$ (at 2σ confidence).

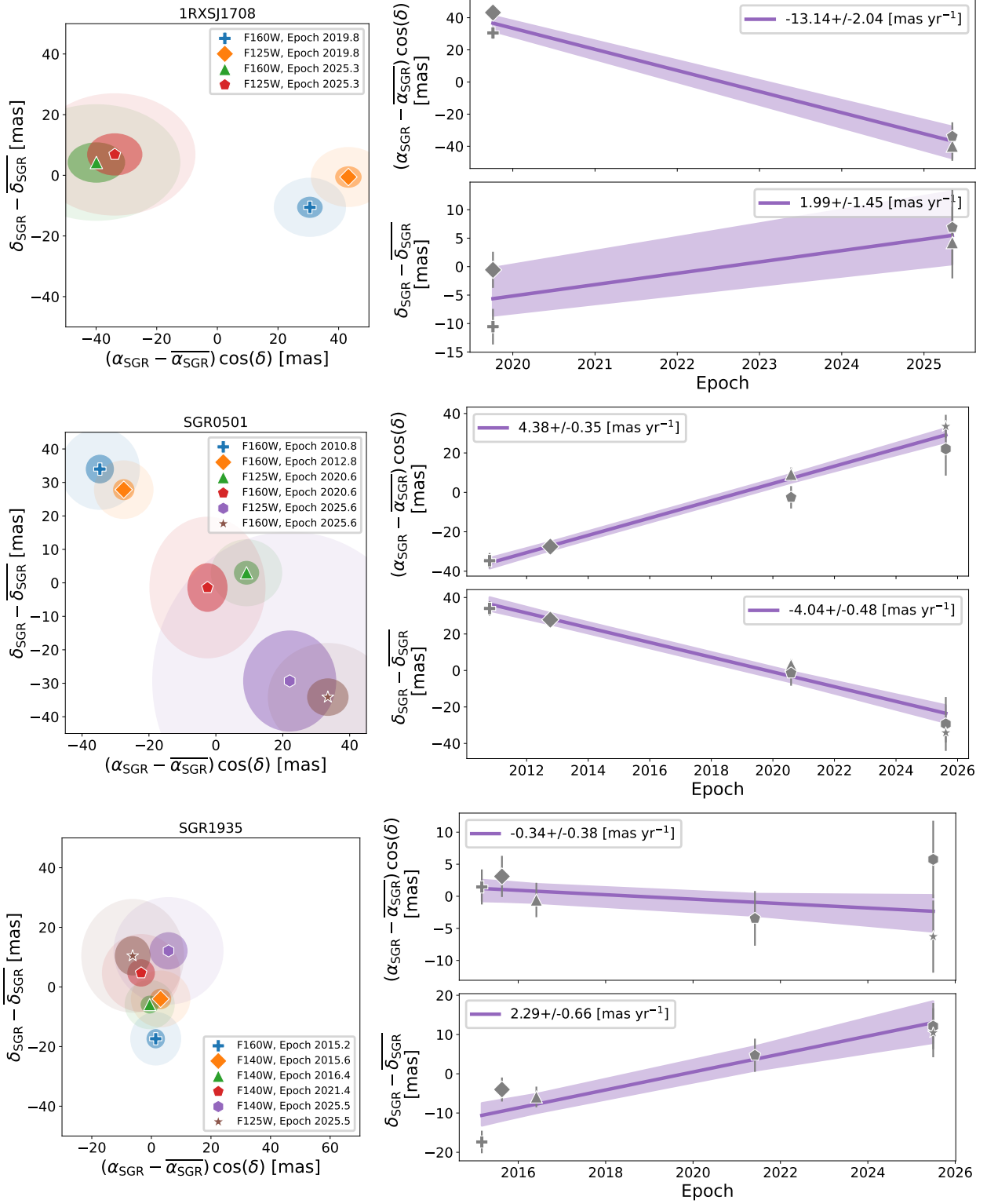


Fig. A.3. Continued as in Figure A.2 for magnetars 1RXSJ 1708, SGR 0501 and SGR 1935.